

Riemannian Flow Matching for Disentangled Graph Domain Adaptation

Yingxu Wang¹ Xinwang Liu² Mengzhu Wang³ Siyang Gao⁴ Nan Yin⁴

Abstract

Graph Domain Adaptation (GDA) typically uses adversarial learning to align graph embeddings in Euclidean space. However, this paradigm suffers from two critical challenges: *Structural Degeneration*, where hierarchical and semantic representations are entangled, and *Optimization Instability*, which arises from oscillatory dynamics of minimax adversarial training. To tackle these issues, we propose DisRFM, a geometry-aware GDA framework that unifies Riemannian embedding and flow-based transport. First, to overcome structural degeneration, we embed graphs into a Riemannian manifold. By adopting polar coordinates, we explicitly disentangle structure (radius) from semantics (angle). Then, we enforce topology preservation through radial Wasserstein alignment and semantic discrimination via angular clustering, thereby preventing feature entanglement and collapse. Second, we address the instability of adversarial alignment by using Riemannian flow matching. This method learns a smooth vector field to guide source features toward the target along geodesic paths, guaranteeing stable convergence. The geometric constraints further guide the flow to maintain the disentangled structure during transport. Theoretically, we prove the asymptotic stability of the flow matching and derive a tighter bound for the target risk. Extensive experiments demonstrate that DisRFM consistently outperforms state-of-the-art methods.

1. Introduction

Graph Domain Adaptation (GDA) facilitates knowledge transfer across graph domains under distribution shifts while preserving task-relevant information (Wu et al., 2020). A central challenge lies in aligning graphs at both representa-

¹The Chinese University of Hong Kong ²National University of Defense Technology ³The Hebei University of Technology ⁴The City University of Hong Kong. Correspondence to: Nan Yin <yinnan8911@gmail.com>.

Preprint. February 3, 2026.

tion and structural levels, ensuring consistent matching of topologically similar graphs (Henderson et al., 2012). Existing methods predominantly align embeddings in Euclidean spaces (Sun et al., 2020; Shen et al., 2020) via adversarial training (Ganin et al., 2016; Feng et al., 2020), which minimizes domain discrepancy by enforcing feature indistinguishability. Despite its efficacy in simple settings, this paradigm often struggles to capture complex structures.

Specifically, we argue that current GDA paradigms suffer from two fundamental issues. First, Euclidean embeddings often lead to *Structural Degeneration* (Bronstein et al., 2017; Nickel & Kiela, 2017). In Euclidean space, structural roles and semantic identity are tightly entangled (Ganea et al., 2018), making it difficult to preserve graph topology during cross-domain alignment. As a result, models are frequently forced to collapse distinct structural patterns in order to satisfy alignment objectives, discarding important topological information (Sala et al., 2018; Chami et al., 2019). Figure 1(a) illustrates how this process leads to degenerated representations that no longer reflect the intrinsic organization of the graph. Second, adversarial alignment introduces severe *Optimization Instability* (Arjovsky et al., 2017; Mescheder et al., 2018). The minimax formulation creates a saddle-point objective in which the feature extractor and discriminator engage in a competitive game (Goodfellow et al., 2014). As shown in Figure 1(c), this interaction often results in oscillatory training dynamics rather than stable convergence (Salimans et al., 2016; Roth et al., 2017). Such instability can misguide representation learning and undermine the reliability of domain-invariant features.

Motivated by these observations, we revisit GDA from first principles by rethinking both the embedding geometry and the alignment mechanism. To address structural degeneration, we note that preserving graph topology requires explicitly separating structural roles from semantic identity (Wang et al., 2024a). Euclidean geometry lacks the capacity to support this separation due to geometric congestion (Bronstein et al., 2017), which forces different types of information to overlap in the same space (Chami et al., 2019). We overcome this limitation by embedding graphs in a Riemannian manifold equipped with polar coordinates, which naturally disentangle structure and semantics (Nickel & Kiela, 2017; Tifrea et al., 2018). In this geometry, structural depth is encoded in the radial component, while se-

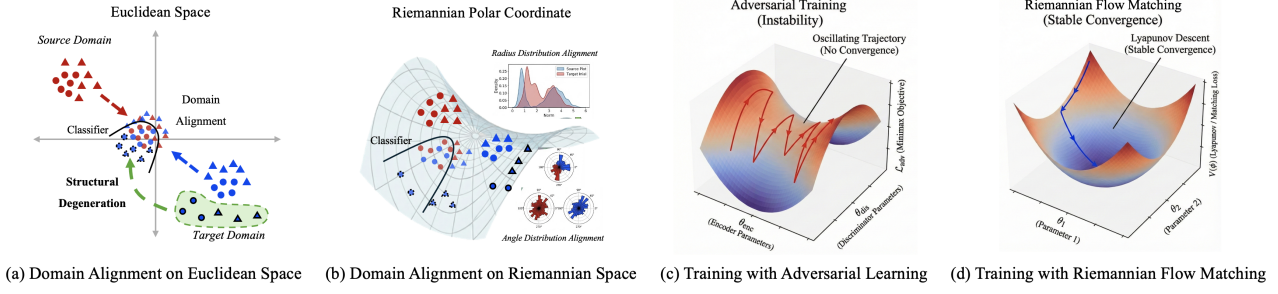


Figure 1. (a) (c) show Structural Degeneration and Optimization Instability in Euclidean adversarial alignment. (b) (d) describe the Riemannian polar coordinates that enable disentangled structure-semantics encoding, while flow matching ensures stable convergence.

semantic identity is captured by the angular component, as illustrated in Figure 1(b). This inductive bias enables semantic alignment across domains without distorting structural roles. To resolve optimization instability, we replace adversarial minmax objectives with a stable flow matching framework (Lipman et al., 2023). Instead of training a discriminator, we directly learn a time-dependent vector field that transports source representations toward the target distribution along smooth geodesic paths. As illustrated in Figure 1(d), this formulation transforms an unstable game into a well-conditioned regression problem, leading to steady and reliable convergence (Liu et al., 2023b).

Based on these principles, we propose DisRFM, a unified framework for geometry-aware and stable graph domain adaptation. DisRFM embeds graphs in a Riemannian polar coordinates, where the radial dimension represents structural hierarchy and the angular dimension encodes semantic identity. Importantly, radial and angular components are intrinsically coupled through the Riemannian metric. Performing alignment independently in each coordinate would break this coupling and yield geometrically inconsistent, non-geodesic trajectories. To avoid this issue, DisRFM performs flow matching in the joint embedding space, learning a single vector field that transports representations along coupled, minimum-energy geodesics. Disentanglement is enforced only through boundary constraints on the endpoint distributions of radius and angle, shaping the source and target embeddings without altering the intermediate geodesic evolution. Theoretically, we show that DisRFM ensures sufficient structural capacity and achieves asymptotic convergence, leading to a tighter generalization bound for GDA. Our main contributions are summarized as follows:

- We identify two critical challenges in GDA paradigms: optimization instability due to minimax dynamics, and structural degeneration driven by Euclidean coupling.
- We propose DisRFM, which integrates Riemannian polar coordinates with flow matching to achieve geometry-aware and stable domain adaptation.
- Extensive experiments on benchmark demonstrate that DisRFM significantly outperforms state-of-the-art baselines, validating the effectiveness of the proposed method.

2. Related Work

Domain Adaptation (DA). DA aims to transfer knowledge from a labeled source domain to an unlabeled target domain by reducing distributional shifts while maintaining task-relevant semantics (Singhal et al., 2023; Xu et al., 2024). With the widespread use of graph data, this approach has extended to Graph Domain Adaptation (GDA), which deals with domain shifts where both node attributes and structures vary (Wu et al., 2024; Wang et al., 2025a). Most current methods use graph neural networks to learn representations and apply alignment techniques, such as adversarial learning, MMD minimization, or optimal transport, to create domain-invariant features (Wang et al., 2024b; Liu et al., 2024b). However, these methods typically align graphs in Euclidean space and fail to consider the underlying non-Euclidean geometry of the data. This often results in distorted representations and negative transfer, especially under significant structural shifts (Yin et al., 2025b; Fang et al., 2025; Chen et al., 2025b). To address this limitation, we propose DisRFM, a framework that performs geometry-aware alignment in non-Euclidean space.

Manifold Learning on Graphs. Manifold learning operates on the premise that high-dimensional data inherently reside on low-dimensional manifolds, enabling the capture of intrinsic geometric properties that Euclidean methods often distort (Lin & Zha, 2008; Zhang et al., 2011; Meilă & Zhang, 2024). Recent advances extend this paradigm to non-Euclidean spaces, integrating graph topology to better encode hierarchical and relational structures (Sun et al., 2025; 2024; Fei et al., 2025). However, existing manifold-based methods predominantly focus on single-domain tasks, overlooking the challenge of domain adaptation (Borde et al., 2022; Sun et al., 2023; Wang et al., 2024c). Crucially, the naive application of general adaptation techniques to manifold spaces proves suboptimal, as these methods fail to model cross-domain distributional shifts while strictly adhering to the underlying geometry (Chen et al., 2025a; Gharib et al., 2025; Collas et al., 2025). To bridge this gap, we propose DisRFM, which formulates graph domain adaptation as a continuous, geometry-aware transformation on a non-Euclidean manifold via Riemannian flow matching.

3. Preliminaries

3.1. Problem Definition

We focus on the problem of GDA for graph classification. Let $\mathcal{D}_S = \{(\mathcal{G}_i^S, y_i^S)\}_{i=1}^{N_S}$ and $\mathcal{D}_T = \{\mathcal{G}_j^T\}_{j=1}^{N_T}$ denote the labeled source and unlabeled target domains. Both of them share a label space \mathcal{Y} but with shifting distributions $\mathbb{P}_S(\mathcal{D}_S) \neq \mathbb{P}_T(\mathcal{D}_T)$. Each graph is represented as $\mathcal{G} = (\mathcal{V}, \mathcal{E}, X)$, where \mathcal{V} is the set of nodes, \mathcal{E} is the set of edges, and $X \in \mathbb{R}^{|\mathcal{V}| \times F}$ denotes the node features. Our goal is to learn a geometry-aware encoder $f_\theta : \mathcal{G} \rightarrow \mathcal{M}_c$ and classifier $g_\phi : \mathcal{M}_c \rightarrow \mathcal{Y}$ to minimize classification error on \mathcal{D}_T , where \mathcal{M}_c is a latent Riemannian manifold.

3.2. Riemannian Graph Convolution.

Following the unified framework of Hyperbolic Graph Neural Networks (HGNN) (Liu et al., 2019), we generalize standard GCNs to a constant curvature Riemannian manifold \mathcal{M}_c . The sign of the curvature c adaptively dictates the underlying geometry, unifying Hyperbolic Space \mathbb{H} ($c < 0$), Euclidean Space \mathbb{E} ($c = 0$), and Spherical Space \mathbb{S} ($c > 0$) spaces within a single formalism. Fundamental operations, such as linear transformation and aggregation, are executed by mapping features to the tangent space $T_0\mathcal{M}_c$, performing Euclidean computations, and retracting the results back to the manifold. Specifically, the linear transformation of a node feature $\mathbf{h}_j^{(l)} \in \mathcal{M}_c$ via a weight matrix $\mathbf{W}^{(l)}$ is defined by Möbius matrix-vector multiplication:

$$\mathbf{m}_j^{(l)} = \mathbf{W}^{(l)} \otimes_c \mathbf{h}_j^{(l)} = \text{Exp}_0^c \left(\mathbf{W}^{(l)} \cdot \text{Log}_0^c(\mathbf{h}_j^{(l)}) \right).$$

Then, neighborhood aggregation is grounded in the Fréchet mean (Karcher, 1977), and approximated in the tangent space, resulting in the unified layer-wise update rule:

$$\mathbf{h}_i^{(l+1)} = \text{Exp}_0^c \left(\sigma \left(\sum_{j \in \mathcal{N}(i) \cup \{i\}} \alpha_{ij} \cdot \text{Log}_0^c(\mathbf{m}_j^{(l)}) \right) \right). \quad (1)$$

This architecture enforces a “Log-Transform-Exp” cycle, ensuring that representation learning faithfully respects the underlying manifold geometry. The details of Riemannian Geometry are introduced in Appendix A.

4. Methodology

4.1. Overview of Framework

In this paper, we propose DisRFM, a geometry-aware framework for GDA, which comprises two core components: (1)

Disentangled Geometric Constraints. We explicitly decouple representations in a Riemannian polar coordinate system by enforcing structural hierarchy via radial Wasserstein matching and semantic discrimination via confidence-gated angular pseudo-label clustering, thereby preconditioning the

latent space for transport. (2) **Geometry-Aware Manifold Transport.**

We formulate domain shift as a continuous Riemannian flow. Learning a geometry-respecting vector field enables smooth, topology-preserving transport to bridge the cross-domain gap. **Theoretically**, we rigorously prove the necessity of Riemannian embeddings via distortion analysis, the asymptotic stability of our manifold flow matching, and a tighter generalization bound on the target risk.

4.2. Disentangled Geometric Constraints

Traditional GDA methods typically operate in Euclidean spaces and incur significant distortion when embedding hierarchical graphs (Nickel & Kiela, 2017; Bronstein et al., 2017). Although Riemannian manifolds offer improved capacity (Chami et al., 2019), simply transplanting standard alignment paradigms is suboptimal. These methods typically operate uniformly on the embedding space, neglecting the intrinsic geometric heterogeneity where the radial component governs structural hierarchy (Nickel & Kiela, 2017) while the angular component encodes semantic identity (Tifrea et al., 2018). To respect this geometric heterogeneity, we propose Disentangled Geometric Constraints. By design, we constrain the radial component via Wasserstein distribution matching to preserve structural hierarchy, and constrain the angular component via confidence-gated clustering to maintain semantic discriminability. This ensures the latent geometry is constructed in strict accordance with the intrinsic physical properties of the Riemannian manifold.

Structural Hierarchy Constraint. First, we obtain the graph-level representation $\mathbf{z} \in \mathcal{M}_c$ via Eq. (1), where the manifold curvature c controls the underlying geometry. To disentangle the geometric properties, we map \mathbf{z} to the tangent space via the Logarithmic map $\mathbf{v} = \text{Log}_0^c(\mathbf{z}) \in T_0\mathcal{M}_c$ and apply orthogonal decomposition to separate the embedding into a radial scalar r and a directional vector \mathbf{u} :

$$r = \|\mathbf{v}\|_2, \quad \mathbf{u} = \frac{\mathbf{v}}{\|\mathbf{v}\|_2},$$

where the radius r serves as a proxy for structural centrality of graphs, while \mathbf{u} retains the semantic orientation required for classification. Unlike holistic methods that indiscriminately entangle geometric and semantic, we explicitly isolate the radial component to enforce a Structural Hierarchy Constraint. Our goal is to calibrate global structural profile of the target domain to match the source, ensuring consistent distributions of topological complexity. We formulate this as a marginal distribution matching problem to calibrate the target’s global topological profile. Formally, we minimize the Wasserstein distance (Courty et al., 2016) between the source and target radial distributions. Leveraging the closed-form solution for univariate measures (Peyré et al., 2019), we efficiently compute this metric via sorting. For a batch of size B , we obtain the order statistics $\mathcal{R}_S = \text{sort}(\{r_S^{(i)}\}_{i=1}^B)$

and $\mathcal{R}_T = \text{sort}(\{r_T^{(i)}\}_{i=1}^B)$, defining the loss as:

$$\mathcal{L}_{RAD} = \frac{1}{B} \sum_{k=1}^B |\mathcal{R}_S[k] - \mathcal{R}_T[k]|. \quad (2)$$

Minimizing \mathcal{L}_{RAD} constrains the global structural profile of the target domain to align with the source. This effectively prevents structural collapse, ensuring intrinsic topological diversity of graphs is preserved during adaptation.

Semantic Discriminative Constraint. Let $\mathbf{W} \in \mathbb{R}^{K \times d}$ denote the source classifier weights, where each row \mathbf{w}_k serves as a prototype for class k . For a target graph with tangent representation $\mathbf{v}_T^{(i)}$, we decouple semantics from structure by normalizing both $\mathbf{v}_T^{(i)}$ and \mathbf{w}_k to unit length:

$$\hat{\mathbf{v}}_T^{(i)} = \frac{\mathbf{v}_T^{(i)}}{\|\mathbf{v}_T^{(i)}\|_2}, \quad \hat{\mathbf{w}}_k = \frac{\mathbf{w}_k}{\|\mathbf{w}_k\|_2}.$$

The semantic similarity is then measured by cosine distance $s_{i,k} = \hat{\mathbf{v}}_T^{(i)} \cdot (\hat{\mathbf{w}}_k)^\top$, ensuring the Semantic Discriminative Constraint is orthogonal to the radial structural constraints.

Ideally, the angular component \mathbf{u} should be constrained to form distinct semantic clusters around class prototypes. However, since target ground-truth labels are unavailable, we rely on the source classifier to generate pseudo-labels for guiding this clustering process (Lee et al., 2013). Recognizing that indiscriminate usage of noisy pseudo-labels risks distorting the manifold geometry (Zou et al., 2018; Chen et al., 2019), we employ a dual-criteria filtering mechanism to enforce the semantic discriminative constraint selectively:

(1) *Confidence Gating*: We generate pseudo-labels \hat{y}_i based on the source classifier. To filter out noisy predictions, we apply a binary mask M_i , which retains samples only if their confidence score exceeds a threshold ζ :

$$M_i = \mathbb{I} \left(\max_k p(k|\mathbf{v}_T^{(i)}) > \zeta \right),$$

where $p(\cdot) = \text{Softmax}(\mathbf{W}\mathbf{v}_T^{(i)})$ denotes the class probability, and $\mathbb{I}(\cdot)$ is the indicator function. This mask M_i retains only samples with confidence exceeding ζ , effectively filtering out uncertain predictions.

(2) *Radial Weighting*: In the geometric space, embeddings with small radii encode generic, shared features which are typically domain-invariant. Conversely, embeddings with large radii capture sample-specific details that are susceptible to domain shift. We assign a geometric reliability weight α_i to prioritize the alignment of these stable representations:

$$\alpha_i = \exp \left(-\|\mathbf{v}_T^{(i)}\|_2 \right).$$

The final objective maximizes the cosine similarity between the direction of confident target samples and their corresponding semantic anchors, weighted by their geometric

stability. The loss is formulated as:

$$\mathcal{L}_{ANG} = \frac{\sum_{i=1}^B M_i \cdot \alpha_i \cdot \ell_{ce}(\gamma \cdot \mathbf{s}_i, \hat{y}_i)}{\sum_{i=1}^B M_i \cdot \alpha_i + \epsilon}, \quad (3)$$

where ℓ_{ce} is the Cross-Entropy loss, \mathbf{s}_i is the vector of cosine similarities, and γ is a temperature scaling factor to sharpen the predictions. By minimizing \mathcal{L}_{ANG} , we enforce semantic consistency in the angular domain while respecting the hierarchical reliability inferred from the radial domain.

4.3. Geometry-Aware Manifold Transport

Existing approaches for GDA predominantly rely on adversarial learning to align source and target distributions (Ganin et al., 2016; Wu et al., 2020; Dai et al., 2022). However, these methods are fundamentally limited by the instability of the minimax optimization objective (Arjovsky & Bottou, 2017; Mescheder et al., 2018). The adversarial interplay between the feature encoder and the domain discriminator often leads to vanishing gradients and difficulty in reaching convergence, making the training process highly volatile (Arjovsky et al., 2017). To circumvent these optimization hurdles, we propose a Geometry-Aware Manifold Transport module that replaces the volatile adversarial game with a stable, continuous flow matching process (Lipman et al., 2023; Zagheni et al., 2025; Huang et al., 2025).

Formally, we model the adaptation as a conditional flow between a source $\mathbf{z}_S \sim \mathbb{P}_S$ and a target $\mathbf{z}_T \sim \mathbb{P}_T$. We define the intermediate state \mathbf{z}_t via geodesic interpolation, leveraging the Riemannian exponential map to ensure energy-minimizing transport on \mathcal{M}_c :

$$\mathbf{z}_t = \gamma_t(\mathbf{z}_S, \mathbf{z}_T) = \text{Exp}_{\mathbf{z}_S}^c(t \cdot \text{Log}_{\mathbf{z}_S}^c(\mathbf{z}_T)).$$

To generate this geodesic flow, we derive the driving vector field \mathbf{u}_t . Leveraging the property that geodesics exhibit zero covariant acceleration, the velocity at any intermediate point \mathbf{z}_t is obtained by parallel transporting the initial velocity. Let $\mathbf{v}_0 = \text{Log}_{\mathbf{z}_S}^c(\mathbf{z}_T) \in T_{\mathbf{z}_S} \mathcal{M}_c$ denote the initial tangent vector. The target vector field is then given by:

$$\mathbf{u}_t(\mathbf{z}_t) = P_{\mathbf{z}_S \rightarrow \mathbf{z}_t}^c(\mathbf{v}_0),$$

where $P_{x \rightarrow y}^c$ denotes the parallel transport operator, preserving the geometric orientation of the flow. To learn the generative trajectory defined by \mathbf{u}_t , we parameterize a time-dependent neural vector field $v_\theta : \mathcal{M}_c \times [0, 1] \rightarrow T\mathcal{M}_c$. The training objective is to regress $v_\theta(\mathbf{z}_t, t)$ onto the analytic geodesic flow \mathbf{u}_t by minimizing the expected Riemannian squared error in the tangent space:

$$\mathcal{L}_{FM} = \mathbb{E}_{t \sim \mathcal{U}[0,1], (\mathbf{z}_S, \mathbf{z}_T) \sim \pi} \left[\|v_\theta(\mathbf{z}_t, t) - \mathbf{u}_t(\mathbf{z}_t)\|_{\mathbf{z}_t}^2 \right]. \quad (4)$$

Here, $\|\cdot\|_{\mathbf{z}_t}$ is the norm induced by the metric $g_{\mathbf{z}_t}^c$. We employ a Class-Conditional Nearest Neighbors coupling strategy π (Tong et al., 2023) to pair semantically similar graphs,

ensuring that v_θ learns to transport source embeddings to the target domain along optimal, geometry-preserving paths.

4.4. Learning Framework

Coupled Dynamics with Decoupled Constraints. The core philosophy of DisRFM is to synergize disentangled geometric structuring with manifold-consistent transport. To achieve this, we distinguish between *optimizing the transport trajectory* and *defining the target geometry*:

- Joint Manifold Transport (Dynamics): We perform flow matching on the joint manifold rather than optimizing radial and angular components separately. In Riemannian space, these dimensions are intrinsically coupled by the metric tensor. Independent optimization would neglect this curvature, effectively treating the space as Euclidean and forcing the transport to follow distorted, high-energy paths. Instead, our unified flow respects this metric-induced coupling, guiding features along energy-minimizing geodesics to ensure optimal transport.
- Disentangled Target Definition (Statics): Conversely, we enforce constraints separately on the marginal distributions of the radius and angle. As proven in Theorem 4.2, the gradient flows of these objectives are orthogonal under the Riemannian metric. This allows us to strictly define the shape of the destination manifold, ensuring radial hierarchy and angular discriminability, without interfering with the dynamics of the transport path.

In summary, the disentangled constraints act as static boundary conditions that define a structurally valid target, while the unified flow acts as the dynamic solver that finds the optimal geodesic path to reach it.

Training Objective. Formally, DisRFM jointly optimizes the source task capability, geometric structural integrity, and the manifold transport trajectory. The total objective function is formulated as:

$$\mathcal{L}_{total} = \mathcal{L}_{task} + \lambda_1 \mathcal{L}_{RAD} + \lambda_2 \mathcal{L}_{ANG} + \lambda_3 \mathcal{L}_{FM}, \quad (5)$$

where λ_1 , λ_2 , and λ_3 are hyper-parameters balancing the contributions of structural alignment, semantic alignment, and manifold transport, respectively. Specifically, \mathcal{L}_{task} is the standard cross-entropy loss computed on the labeled source domain \mathcal{D}_S to ensure discriminative capability:

$$\mathcal{L}_{task} = \mathbb{E}_{(\mathbf{v}_S, y_S) \sim \mathcal{D}_S} [-\log p(y_S | \mathbf{v}_S)],$$

where $p(y | \mathbf{v}_S) = \text{Softmax}(\mathbf{W}\mathbf{v}_S + \mathbf{b})$ denotes the predicted probability in the tangent space.

4.5. Theoretical Analysis

In this section, we provide rigorous theoretical justifications for DisRFM. We analyze the necessity of the Riemannian

polar geometry for disentanglement, prove the convergence stability of our flow matching objective, and derive a tighter generalization bound for the target domain risk.

Geometric Disentanglement Capacity. DisRFM operates on a general Riemannian polar space which can instantiate into Euclidean (\mathbb{E}), Spherical (\mathbb{S}), or Hyperbolic (\mathbb{H}) geometries depending on the curvature c . We first analyze the volume growth properties of these spaces to justify the necessity of negative curvature for hierarchical embedding.

Proposition 4.1 (Exponential Volume Expansion). *Let $\text{Vol}(\mathcal{B}_X(R))$ denote the volume of a ball with radius R in a geometric space $X \in \{\mathbb{E}, \mathbb{S}, \mathbb{H}\}$. As $R \rightarrow \infty$, the volume growth behaviors diverge significantly:*

- **Spherical ($\mathbb{S}, c > 0$):** The volume is finite and periodic, scaling as $\sin^{d-1}(\sqrt{c}R)$.
- **Euclidean ($\mathbb{E}, c = 0$):** The volume grows polynomially, scaling as R^{d-1} .
- **Hyperbolic ($\mathbb{H}, c < 0$):** The volume expands exponentially, satisfying:

$$\lim_{R \rightarrow \infty} \frac{\text{Vol}(\mathcal{B}_{\mathbb{H}}(R))}{\exp((d-1)\sqrt{|c|}R)} = \text{const} > 0.$$

The proof is detailed in Appendix B. This proposition highlights the unique advantage of the Hyperbolic component within our framework. While Euclidean (\mathbb{E}) and spherical (\mathbb{S}) spaces are constrained by polynomial and finite volume growth, only hyperbolic space (\mathbb{H}) offers the exponential capacity required to embed hierarchical graph structures with arbitrarily low distortion. This theoretical insight rigorously grounds our architectural choice to incorporate negative curvature in the radial dimension explicitly.

Theorem 4.2 (Disentanglement Efficiency via Metric Orthogonality). *Consider the optimization dynamics in the Riemannian polar coordinate system (r, θ) with metric tensor g . The gradient flows for structural preservation ($\nabla_r \mathcal{L}$) and semantic alignment ($\nabla_\theta \mathcal{L}$) are **orthogonal** under the Riemannian metric:*

$$\langle \nabla_r \mathcal{L}, \nabla_\theta \mathcal{L} \rangle_g = 0.$$

Furthermore, the available semantic capacity (angular space) at depth r scales as $\sinh^{d-1}(\sqrt{|c|}r)$.

The details are provided in Appendix C. Theorem 4.2 provides the theoretical guarantee for our “Disentangled Alignment” module. The orthogonality condition ensures that when the model updates the angular component to align semantic classes across domains, it generates *zero projection* onto the radial component. This means we can aggressively align semantic distributions without inadvertently destroying the hierarchical structure encoded in the radius, solving the “entanglement” problem inherent in Euclidean methods.

Stability Analysis. We contrast the optimization landscape of DisRFM with standard adversarial alignment (adversarial-based GDA), which relies on a minimax game.

Theorem 4.3 (Spectral Instability of Adversarial Training). *Let $\omega^* = (\theta^*, \phi^*)$ be a local Nash equilibrium of the adversarial objective. If the local curvature is dominated by the interaction term between the generator and discriminator, the Jacobian matrix of the gradient vector field at ω^* possesses purely imaginary eigenvalues ($\text{Re}(\lambda) = 0, \text{Im}(\lambda) \neq 0$).*

The proof is presented in Appendix D. In dynamical systems theory, a fixed point with purely imaginary eigenvalues is classified as a center, not an attractor (Strogatz, 2001; Mescheder et al., 2017). This theorem reveals the root cause of training instability in adversarial-based GDA: the system tends to form closed orbits (limit cycles) around the equilibrium rather than converging to it. This explains the persistent oscillations and difficulty in model selection often encountered in adversarial adaptation methods.

Theorem 4.4 (Asymptotic Stability of DisRFM). *The optimization dynamics of DisRFM, governed by the flow matching objective \mathcal{L}_{FM} , follow a conservative gradient field. \mathcal{L}_{FM} acts as a strict Lyapunov function for the system:*

$$\frac{d}{dt} \mathcal{L}_{FM}(\theta(t)) = -\|\nabla_{\theta} \mathcal{L}_{FM}\|^2 \leq 0.$$

The details of the proof are presented in Appendix E. Unlike the adversarial game, Theorem 4.4 proves that our Flow Matching objective transforms the adaptation problem into a stable regression task. By ensuring that the “energy” (loss) of the system is strictly non-increasing along the optimization trajectory, DisRFM structurally precludes limit cycles and guarantees asymptotic convergence to the set of stationary points, providing a reliable and robust training process.

Generalization Bound. Finally, we connect the geometric and optimization advantages to the generalization performance on the target domain. Based on the domain adaptation theory (Ben-David et al., 2010), the target risk $\epsilon_T(h)$ is bounded by the source risk $\epsilon_S(h)$ plus a divergence term.

Theorem 4.5 (Tighter Generalization Bound). *Let \mathcal{H} be a hypothesis space of graph classifiers. For any hypothesis $h \in \mathcal{H}$, let $\epsilon_S(h)$ and $\epsilon_T(h)$ denote its expected risk on the source domain \mathcal{D}_S and target domain \mathcal{D}_T , respectively. According to the domain adaptation theory (Ben-David et al., 2010), the target risk is bounded by:*

$$\epsilon_T(h) \leq \epsilon_S(h) + \frac{1}{2} \hat{d}_{\mathcal{H}\Delta\mathcal{H}}(\mathcal{D}_S, \mathcal{D}_T) + C,$$

where $\hat{d}_{\mathcal{H}\Delta\mathcal{H}}$ is the realized divergence and C is a constant. The DisRFM achieves a strictly tighter bound on the divergence term than Euclidean-Adversarial baselines (Base):

$$\hat{d}_{DisRFM} \leq \hat{d}_{Base} - \underbrace{\Omega(n^{1/d})}_{\Delta_{geo}} - \underbrace{\xi_{opt}}_{\Delta_{opt}},$$

where n is the number of nodes in the graph hierarchy, d is the embedding dimension, and $\xi_{opt} > 0$ represents the irreducible optimization gap caused by adversarial instability. Consequently, Δ_{geo} and Δ_{opt} quantify the reductions in geometric distortion and optimization error, respectively.

The proof is presented in Appendix F. Theorem 4.5 unifies our contributions into a performance guarantee. The term Δ_{geo} represents the irreducible error caused by Euclidean distortion, which our hyperbolic embedding eliminates. The term Δ_{opt} represents the residual divergence caused by adversarial non-convergence, which our stable flow matching closes. These reductions theoretically certify that DisRFM can achieve lower target risk than existing paradigms.

5. Experiments

5.1. Experimental Settings

Dataset. We evaluate DisRFM on two types of domain shift scenarios: (1) structure-based domain shifts: we partition the PROTEINS, NCI1, Mutagenicity (Dobson & Doig, 2003), and ogbg-molhiv (Hu et al., 2021) datasets based on node and edge densities, following the protocol described in (Yin et al., 2025a); (2) feature-based domain shifts: we evaluate DisRFM on DD, PROTEINS, BZR, BZR_MD, COX2, and COX2_MD (Sutherland et al., 2003) datasets. The statistics, distribution visualization, and detailed introduction of experimental datasets are shown in Appendix G.

Baselines. We compare DisRFM with competitive baselines on above datasets, including two graph kernel methods: WL subtree (Shervashidze et al., 2011) and PathNN (Michel et al., 2023); four general graph neural networks: GCN (Kipf & Welling, 2017), GIN (Xu et al., 2018), CIN (Bodnar et al., 2021) and GMT (Baek et al., 2021); four manifold-based graph neural networks: dDGM (Borde et al., 2022), RieGrace (Sun et al., 2023), ProGDM (Wang et al., 2024c), and D-GCN (Sun et al., 2024); seven graph domain adaptation methods: DEAL (Yin et al., 2022), SGDA (Qiao et al., 2023), StruRW (Liu et al., 2023a), A2GNN (Liu et al., 2024a), PA-BOTH (Liu et al., 2024b), GAA (Fang et al., 2025), and TDSS (Chen et al., 2025b); and three manifold-based domain adaptation methods: GOTDA (Long et al., 2022), MASH (Rustad et al., 2024), and GeoAdapt (Gharib et al., 2025). More details are introduced in Appendix H.

Implementation Details. We implement DisRFM in PyTorch and conduct all experiments on NVIDIA A100 GPUs to ensure fair comparison. For the encoder architecture, DisRFM adopts HGNC (Liu et al., 2019) as the backbone, enabling adaptive representation learning across different Riemannian spaces (hyperbolic, Euclidean, or spherical) by modulating the curvature parameter c . All experiments are conducted under identical hyperparameter settings, using the Adam optimizer with a learning rate of 1×10^{-4} , a

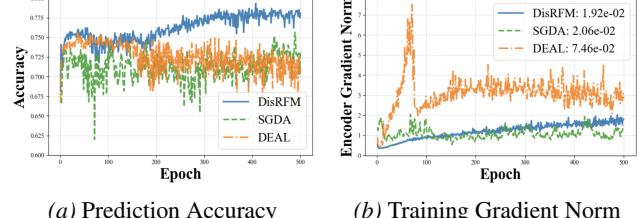
Table 1. Graph classification results (in %) under node and edge density domain shifts on the Mutagenicity dataset, and feature domain shifts on DD, PROTEINS, BZR, BZR.MD, COX2, and COX2.MD. For convenience, PROTEINS, DD, COX2, COX2.MD, BZR, and BZR.MD are abbreviated as P, D, C, CM, B, and BM, respectively. **Bold** results indicate the best performance.

Methods	Node Shift			Edge Shift			Feature Shift					
	M0→M1	M0→M2	M0→M3	M0→M1	M0→M2	M0→M3	P→D	D→P	C→CM	CM→C	B→BM	BM→B
WL subtree	34.3	40.4	52.7	34.4	47.6	52.7	43.0	42.2	53.1	58.2	51.3	44.0
GCN	64.1±1.4	65.5±2.0	56.9±2.1	66.3±1.7	63.6±1.4	56.0±1.4	48.9±2.0	60.9±2.3	51.2±1.8	66.9±1.8	48.7±2.0	78.8±1.7
GIN	66.5±2.1	52.0±1.7	53.7±1.7	67.1±1.7	54.2±2.6	55.4±1.9	57.3±2.2	61.9±1.9	53.8±2.5	55.6±2.0	49.9±2.4	79.2±2.8
GMT	65.7±1.8	62.1±2.1	59.0±2.0	67.9±1.3	61.5±1.8	58.2±2.4	59.5±2.5	50.7±2.2	49.3±1.8	58.2±2.0	50.2±2.3	74.4±1.8
CIN	65.1±1.7	66.0±1.7	55.2±1.5	66.3±1.8	60.8±1.7	55.8±2.4	59.1±2.6	58.0±2.7	51.2±2.0	55.6±1.5	49.2±1.4	74.2±1.9
PathNN	70.2±1.5	67.1±2.0	58.0±1.9	68.9±1.9	62.9±1.7	58.1±1.6	57.9±1.8	53.8±3.3	49.8±1.7	66.9±2.5	50.3±2.3	75.3±2.2
dDGM	79.1±0.4	70.3±0.5	63.9±0.3	76.5±1.3	69.0±1.3	67.0±0.4	59.0±1.8	63.3±1.5	58.4±2.7	74.3±1.2	53.6±1.6	79.2±1.5
RieGrace	78.5±1.3	70.6±1.4	62.8±1.3	76.4±0.5	68.9±0.6	66.1±1.2	59.8±1.4	63.8±1.3	56.8±2.1	66.6±1.4	52.2±2.3	78.9±2.0
ProGDM	75.2±1.2	69.0±1.1	55.7±1.4	74.6±1.2	67.5±1.2	55.5±0.7	58.7±2.0	59.6±2.3	54.2±1.7	75.2±2.0	52.6±1.3	75.4±2.9
D-GCN	75.2±0.5	67.9±0.4	56.3±1.1	73.8±1.2	66.8±1.4	56.7±1.0	62.4±1.9	59.7±2.1	53.7±1.8	77.6±1.9	51.7±1.6	75.7±2.0
DEAL	77.1±0.9	70.9±0.9	60.3±1.1	76.6±1.6	70.6±1.2	60.2±2.1	61.7±2.0	60.0±1.5	52.7±2.7	69.4±2.9	52.4±2.9	78.6±1.4
SGDA	77.5±0.6	69.7±0.5	65.5±0.8	75.9±1.6	68.9±0.8	64.4±0.4	48.3±2.0	55.8±2.6	49.8±1.8	66.9±2.3	50.3±2.1	78.8±2.6
A2GNN	73.5±1.9	66.1±1.5	60.4±1.1	69.5±1.4	68.6±1.4	58.8±2.2	57.8±2.1	60.3±1.5	51.5±1.8	67.7±2.1	51.6±2.3	77.5±1.9
StruRW	78.3±1.3	69.7±1.3	62.6±0.7	76.1±1.5	69.0±1.3	62.1±1.0	59.1±2.3	58.8±2.8	51.2±2.0	54.8±2.9	49.2±1.4	74.7±2.1
PA-BOTH	69.8±1.5	63.8±1.9	55.3±1.1	74.7±1.1	65.3±1.3	52.2±1.5	54.2±3.2	56.7±2.6	52.9±2.8	61.8±2.0	47.5±3.0	78.8±1.9
GAA	79.3±1.2	71.2±0.7	65.6±1.3	77.5±1.2	70.0±1.2	66.5±1.3	62.4±0.6	64.1±0.8	59.4±1.8	78.4±1.2	57.2±3.3	78.5±3.0
TDSS	63.6±1.3	56.7±1.6	54.7±1.0	71.6±1.5	67.3±1.0	55.4±1.6	61.9±1.1	63.6±1.9	56.8±1.3	77.0±2.6	56.6±1.1	79.1±2.4
GOTDA	77.3±1.3	69.9±1.7	65.3±1.2	76.1±1.2	68.5±0.8	65.8±0.6	62.1±1.5	63.2±1.7	58.5±2.1	78.2±1.1	57.0±1.7	78.9±2.6
MASH	76.1±1.3	66.9±1.3	54.3±1.2	74.4±1.2	66.1±0.5	52.2±1.2	61.8±2.1	64.2±2.4	56.2±2.0	77.2±2.1	55.2±2.0	78.1±2.3
GeoAdapt	76.9±1.5	68.7±1.4	60.1±1.3	75.5±1.2	67.5±1.2	60.5±0.6	63.1±1.2	64.0±1.4	56.7±1.7	78.3±2.1	57.5±2.7	78.5±2.2
DisRFM- \mathbb{E}^n	79.4±0.7	71.0±1.0	65.2±0.2	77.6±0.4	70.2±1.2	66.1±0.3	61.9±1.0	63.0±2.0	56.5±1.9	78.2±1.0	56.8±2.4	78.9±1.3
DisRFM- \mathbb{S}^n	79.7±0.7	72.0±1.0	65.9±0.9	78.0±0.5	71.0±0.6	68.2±1.0	63.8±1.2	64.0±2.7	59.7±1.4	78.4±2.1	57.5±1.8	79.1±1.0
DisRFM- \mathbb{H}^n	79.8±0.8	71.7±0.7	66.7±0.8	78.3±0.7	71.3±0.4	67.7±0.9	63.3±1.3	64.4±1.6	58.3±2.2	79.0±2.5	58.0±1.9	79.4±1.7

weight decay of 1×10^{-12} , a hidden embedding dimension of 128, and three GNN layers. Additionally, we set the manifold curvature $c = -1.0$, the confidence threshold $\zeta = 0.7$, and $\lambda_1 = \lambda_2 = \lambda_3 = 0.1$. Following the same settings (Wu et al., 2020; Yin et al., 2022), DisRFM is trained on labeled source data and evaluated on unlabeled target data. We report classification accuracy for TUDataset benchmarks (e.g., PROTEINS, NCI1) and AUC scores for OGB datasets (e.g., ogbg-molhiv), with all results averaged over five independent runs.

5.2. Performance Comparison

We evaluate DisRFM against all baselines under diverse domain shifts. The detailed results on different datasets are provided in Tables 1 and 8–15. From these results, we observe that: (1) Manifold-based GNNs outperform general GNNs in most cases, confirming the advantage of modeling graphs in non-Euclidean spaces. By using curved geometries, these methods can better capture hierarchical and relational structures, resulting in more expressive representations than those learned in isotropic Euclidean space. (2) The proposed DisRFM consistently outperforms baselines in most cases. We attribute this to two core mechanisms: First, Riemannian Flow Matching replaces volatile adversarial minimax games with a stable regression objective. This ensures convergence to an optimal transport plan, directly translating to superior alignment fidelity. Second, by explicitly separating structural hierarchy from semantic identity, we prevent the feature collapse common in entangled representations. (3) The Hyperbolic variant (DisRFM- \mathbb{H}^n) achieves the best



(a) Prediction Accuracy (b) Training Gradient Norm

Figure 2. Training stability comparisons.

performance in 8 out of 12 scenarios. This supports our theoretical analysis in Proposition 4.1, validating that hyperbolic space's exponential growth is vital for handling hierarchies with minimal distortion. It effectively avoids the capacity limits of Euclidean space. Furthermore, this success proves that Riemannian Flow Matching leverages metric coupling, forcing transport trajectories to respect the graph topology. More results and analysis on other datasets can be found in Appendix J.1

5.3. Training Stability Analysis

To validate the stability of DisRFM, we compare its training dynamics with adversarial baselines (DEAL and SGDA) in Figure 2. As shown in Figure 2(a), DisRFM achieves a smooth and steady accuracy curve. In contrast, the baselines exhibit severe oscillations, which are typical of unstable minimax games. This advantage is further supported by the gradient analysis in Figure 2(b). DisRFM maintains stable gradients with minimal variance ($\sigma^2 \approx 1.92 \times 10^{-2}$). However, DEAL shows gradient explosion and large fluctuations ($\sigma^2 \approx 7.46 \times 10^{-2}$). These results confirm that replacing

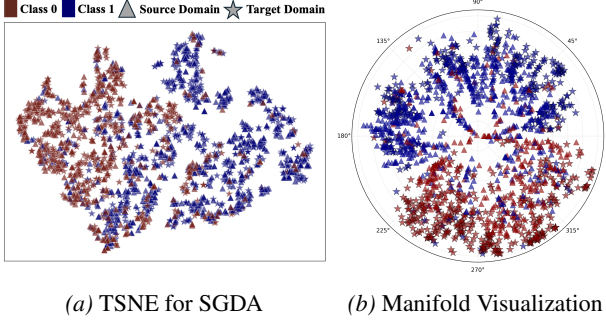


Figure 3. Visualization of TSNE and Manifold Geometry.

the unstable adversarial objective with a stable regression task effectively ensures training stability.

5.4. Visualization of Manifold Geometry

To qualitatively validate the efficacy of our geometric disentanglement strategy, we visualize the learned feature spaces in Figure 3. The traditional baseline (SGDA) suffers from severe feature entanglement, where semantic clusters are indiscriminately crowded and decision boundaries are blurred, indicating a failure to distinguish structural complexities. In contrast, DisRFM achieves explicit structural-semantic disentanglement: semantic categories are distinctively separated along the angular axis, while hierarchical structures are organized along the radial axis. This confirms that DisRFM significantly outperforms traditional baselines by effectively decoupling semantic semantics from structural topology.

Table 2. The results of ablation studies on the Mutagenicity dataset (source \rightarrow target). **Bold** results indicate the best performance.

Methods	M0 \rightarrow M1	M1 \rightarrow M0	M0 \rightarrow M2	M2 \rightarrow M0	M0 \rightarrow M3	M3 \rightarrow M0
DisRFM w/o FM	76.2	73.6	69.6	74.0	65.3	66.2
DisRFM w/o RA	76.9	74.4	70.7	73.9	66.1	67.1
DisRFM w/o AA	76.4	74.0	70.2	73.5	65.7	66.0
DisRFM w/o PE	75.9	72.9	69.0	72.5	64.6	64.8
DisRFM	78.3	76.3	71.3	76.1	67.7	69.2

5.5. Ablation Study

To examine the contribution of each component in DisRFM, we conduct ablation studies on four variants: 1) DisRFM w/o FM, which removes the flow-based transport mechanism; 2) DisRFM w/o RA, which excludes the radial alignment loss; 3) DisRFM w/o AA, which excludes the angular alignment loss; and 4) DisRFM w/o PE, which disables the polar disentanglement strategy entirely. The results are reported in Table 2, and we find the following insights: (1) DisRFM outperforms DisRFM w/o FM, confirming that flow-based transport provides essential principled trajectory guidance to bridge domain discrepancies. (2) The performance drops in DisRFM w/o RA and DisRFM w/o AA validate the necessity of independent geometric constraints. (3) DisRFM w/o PE exhibits the sharpest degradation, underscoring that the joint disentanglement of structural and semantic components is critical for robust graph adaptation.

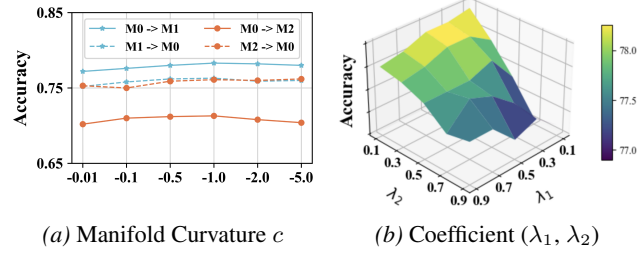


Figure 4. Sensitivity analysis of manifold curvature c and balance coefficient (λ_1, λ_2) on the Mutagenicity dataset.

More results are reported in Appendix J.2.

5.6. Sensitivity Analysis

We conduct a sensitivity analysis of manifold curvature c and balance coefficient (λ_1, λ_2) , and the results are shown in Figure 4. As illustrated in Figure 4(a), the model achieves the best performance at $c = -1.0$. This highlights a key trade-off where the curvature close to 0 fails to capture complex hierarchies due to limited capacity in Euclidean space, while excessively large curvature causes geometric distortion that hurts the representation quality. Therefore, we choose $c = -1.0$ as the default curvature. In parallel, we set $\lambda_3 = 0.1$, and test the performance with (λ_1, λ_2) various between $(0.1, 0.9)$. Figure 4(b) shows that DisRFM’s performance reaches its optimum when $\lambda_1 = 0.1$ and $\lambda_2 = 0.1$. However, accuracy drops significantly as these weights increase, suggesting that while geometric alignment is beneficial, assigning it excessive weight overwhelms the primary classification objective, leading to suboptimal adaptation. More hyperparameter analysis is presented in Appendix J.3.

6. Conclusion

In this paper, we present DisRFM, a geometry-aware framework that addresses the structural degeneration and optimization instability in Euclidean adversarial GDA paradigms. Specifically, we impose disentangled geometric constraints via radial Wasserstein alignment for topological preservation and confidence-gated angular clustering for semantic discrimination to strictly define the target manifold structure. Simultaneously, we replace the volatile minimax game with a stable flow matching objective, which drives source distributions toward the target along energy-minimizing geodesics. This objective avoids oscillatory dynamics, guaranteeing asymptotic stability via Lyapunov analysis and tighter generalization bounds. Extensive experiments show that DisRFM significantly outperforms state-of-the-art methods in both accuracy and stability. In future work, we aim to explore adaptive curvature learning mechanisms for multi-scale structures and extend this Riemannian flow-based framework to heterogeneous graph domain adaptation and generative tasks for scientific discovery.

References

Ajakan, H., Germain, P., Larochelle, H., Laviolette, F., and Marchand, M. Domain-adversarial neural networks. *arXiv preprint arXiv:1412.4446*, 2014.

Arjovsky, M. and Bottou, L. Towards principled methods for training generative adversarial networks. In *International Conference on Learning Representations*, 2017.

Arjovsky, M., Chintala, S., and Bottou, L. Wasserstein generative adversarial networks. In *Proceedings of the International Conference on Machine Learning*, pp. 214–223. PMLR, 2017.

Baek, J., Kang, M., and Hwang, S. J. Accurate learning of graph representations with graph multiset pooling. *arXiv preprint arXiv:2102.11533*, 2021.

Ben-David, S., Blitzer, J., Crammer, K., Kulesza, A., Pereira, F., and Vaughan, J. W. A theory of learning from different domains. *Machine learning*, 79(1):151–175, 2010.

Bodnar, C., Frasca, F., Otter, N., Wang, Y., Lio, P., Montufar, G. F., and Bronstein, M. Weisfeiler and lehman go cellular: Cw networks. *Proceedings of the Conference on Neural Information Processing Systems*, 34:2625–2640, 2021.

Borde, H. S. d. O., Kazi, A., Barbero, F., and Liò, P. Latent graph inference using product manifolds. *arXiv preprint arXiv:2211.16199*, 2022.

Bronstein, M. M., Bruna, J., LeCun, Y., Szlam, A., and Vandergheynst, P. Geometric deep learning: going beyond euclidean data. *IEEE Signal Processing Magazine*, 34(4):18–42, 2017.

Chami, I., Ying, Z., Ré, C., and Leskovec, J. Hyperbolic graph convolutional neural networks. *Proceedings of the Conference on Neural Information Processing Systems*, 32, 2019.

Chen, C., Xie, W., Huang, W., Rong, Y., Ding, X., Huang, Y., Xu, T., and Huang, J. Progressive feature alignment for unsupervised domain adaptation. In *Proceedings of the IEEE/CVF Conference on Computer Vision and Pattern Recognition*, pp. 627–636, 2019.

Chen, D., Xue, S., Chen, L., Wang, Y., Liu, Q., Wu, S., Ma, Z.-M., and Wang, L. Graffe: Graph representation learning via diffusion probabilistic models. *arXiv preprint arXiv:2505.04956*, 2025a.

Chen, W., Ye, G., Wang, Y., Zhang, Z., Zhang, L., Wang, D., Zhang, Z., and Zhuang, F. Smoothness really matters: A simple yet effective approach for unsupervised graph domain adaptation. In *Proceedings of the AAAI Conference on Artificial Intelligence*, volume 39, pp. 15875–15883, 2025b.

Collas, A., Ju, C., Salvy, N., and Thirion, B. Riemannian flow matching for brain connectivity matrices via pull-back geometry. *arXiv preprint arXiv:2505.18193*, 2025.

Courty, N., Flamary, R., Tuia, D., and Rakotomamonjy, A. Optimal transport for domain adaptation. *IEEE transactions on pattern analysis and machine intelligence*, 39(9):1853–1865, 2016.

Dai, Q., Wu, X.-M., Xiao, J., Shen, X., and Wang, D. Graph transfer learning via adversarial domain adaptation with graph convolution. *IEEE Transactions on Knowledge and Data Engineering*, 35(5):4908–4922, 2022.

Dobson, P. D. and Doig, A. J. Distinguishing enzyme structures from non-enzymes without alignments. *Journal of molecular biology*, 330(4):771–783, 2003.

Fang, R., Li, B., Kang, Z., Zeng, Q., Dashtbayaz, N. H., Pu, R., Wang, B., and Ling, C. On the benefits of attribute-driven graph domain adaptation. *arXiv preprint arXiv:2502.06808*, 2025.

Fei, Y., Liu, Y., Jia, C., Li, Z., Wei, X., and Chen, M. A survey of geometric optimization for deep learning: from euclidean space to riemannian manifold. *ACM Computing Surveys*, 57(5):1–37, 2025.

Feng, W., Zhang, J., Dong, Y., Han, Y., Luan, H., Xu, Q., Yang, Q., Kharlamov, E., and Tang, J. Graph random neural networks for semi-supervised learning on graphs. *Advances in neural information processing systems*, 33:22092–22103, 2020.

Ganea, O., Bécigneul, G., and Hofmann, T. Hyperbolic neural networks. *Advances in neural information processing systems*, 31, 2018.

Ganin, Y., Ustinova, E., Ajakan, H., Germain, P., Larochelle, H., Laviolette, F., March, M., and Lempitsky, V. Domain-adversarial training of neural networks. *Journal of machine learning research*, 17(59):1–35, 2016.

Gharib, S., Hartmann, M., and Klami, A. Geometric moment alignment for domain adaptation via siegel embeddings. *arXiv preprint arXiv:2510.14666*, 2025.

Goodfellow, I. J., Pouget-Abadie, J., Mirza, M., Xu, B., Warde-Farley, D., Ozair, S., Courville, A., and Bengio, Y. Generative adversarial nets. *Advances in neural information processing systems*, 27, 2014.

Henderson, K., Gallagher, B., Eliassi-Rad, T., Tong, H., Basu, S., Akoglu, L., Koutra, D., Faloutsos, C., and Li, L. Rolx: structural role extraction & mining in large graphs.

In *Proceedings of the 18th ACM SIGKDD international conference on Knowledge discovery and data mining*, pp. 1231–1239, 2012.

Hu, W., Fey, M., Ren, H., Nakata, M., Dong, Y., and Leskovec, J. Ogb-lsc: A large-scale challenge for machine learning on graphs. *arXiv preprint arXiv:2103.09430*, 2021.

Huang, X., Ruan, T., Zhang, C., and Zhang, S. Graph generation with spectral geodesic flow matching. *arXiv preprint arXiv:2510.02520*, 2025.

Karcher, H. Riemannian center of mass and mollifier smoothing. *Communications on pure and applied mathematics*, 30(5):509–541, 1977.

Kazius, J., McGuire, R., and Bursi, R. Derivation and validation of toxicophores for mutagenicity prediction. *Journal of medicinal chemistry*, 48(1):312–320, 2005.

Khalil, H. K. and Grizzle, J. W. *Nonlinear systems*, volume 3. Prentice hall Upper Saddle River, NJ, 2002.

Kipf, T. N. and Welling, M. Semi-supervised classification with graph convolutional networks. In *Proceedings of the International Conference on Learning Representations*, 2017.

Lee, D.-H. et al. Pseudo-label: The simple and efficient semi-supervised learning method for deep neural networks. In *Workshop on challenges in representation learning, ICML*, volume 3, pp. 896. Atlanta, 2013.

Lin, T. and Zha, H. Riemannian manifold learning. *IEEE transactions on pattern analysis and machine intelligence*, 30(5):796–809, 2008.

Lipman, Y., Chen, R. T. Q., Ben-Hamu, H., Nickel, M., and Le, M. Flow matching for generative modeling. In *The Eleventh International Conference on Learning Representations*, 2023.

Liu, M., Fang, Z., Zhang, Z., Gu, M., Zhou, S., Wang, X., and Bu, J. Rethinking propagation for unsupervised graph domain adaptation. *Proceedings of the AAAI Conference on Artificial Intelligence*, pp. 13963–13971, 2024a.

Liu, Q., Nickel, M., and Kiela, D. Hyperbolic graph neural networks. *Advances in neural information processing systems*, 32, 2019.

Liu, S., Li, T., Feng, Y., Tran, N., Zhao, H., Qiu, Q., and Li, P. Structural re-weighting improves graph domain adaptation. In *Proceedings of the International Conference on Machine Learning*, pp. 21778–21793. PMLR, 2023a.

Liu, S., Zou, D., Zhao, H., and Li, P. Pairwise alignment improves graph domain adaptation. *Proceedings of the International Conference on Machine Learning*, 2024b.

Liu, X., Gong, C., and qiang liu. Flow straight and fast: Learning to generate and transfer data with rectified flow. In *The Eleventh International Conference on Learning Representations*, 2023b.

Long, M., Cao, Z., Wang, J., and Jordan, M. I. Conditional adversarial domain adaptation. *Proceedings of the Conference on Neural Information Processing Systems*, 31, 2018.

Long, T., Sun, Y., Gao, J., Hu, Y., and Yin, B. Domain adaptation as optimal transport on grassmann manifolds. *IEEE Transactions on Neural Networks and Learning Systems*, 34(10):7196–7209, 2022.

Meilă, M. and Zhang, H. Manifold learning: What, how, and why. *Annual Review of Statistics and Its Application*, 11(1):393–417, 2024.

Mescheder, L., Nowozin, S., and Geiger, A. The numerics of gans. *Advances in neural information processing systems*, 30, 2017.

Mescheder, L., Geiger, A., and Nowozin, S. Which training methods for gans do actually converge? In *International conference on machine learning*, pp. 3481–3490. PMLR, 2018.

Michel, G., Nikolentzos, G., Lutzeyer, J. F., and Vazirgiannis, M. Path neural networks: Expressive and accurate graph neural networks. In *Proceedings of the International Conference on Machine Learning*, pp. 24737–24755. PMLR, 2023.

Nickel, M. and Kiela, D. Poincaré embeddings for learning hierarchical representations. *Advances in neural information processing systems*, 30, 2017.

Peyré, G., Cuturi, M., et al. Computational optimal transport: With applications to data science. *Foundations and Trends® in Machine Learning*, 11(5-6):355–607, 2019.

Qiao, Z., Luo, X., Xiao, M., Dong, H., Zhou, Y., and Xiong, H. Semi-supervised domain adaptation in graph transfer learning. In *Proceedings of the International Joint Conference on Artificial Intelligence*, pp. 2279–2287, 2023.

Roth, K., Lucchi, A., Nowozin, S., and Hofmann, T. Stabilizing training of generative adversarial networks through regularization. *Advances in neural information processing systems*, 30, 2017.

Rustad, A. G. et al. Graph integration for diffusion-based manifold alignment. In *2024 International Conference on*

Machine Learning and Applications (ICMLA), pp. 1–8. IEEE, 2024.

Sala, F., De Sa, C., Gu, A., and Ré, C. Representation tradeoffs for hyperbolic embeddings. In *International conference on machine learning*, pp. 4460–4469. PMLR, 2018.

Salimans, T., Goodfellow, I., Zaremba, W., Cheung, V., Radford, A., and Chen, X. Improved techniques for training gans. *Advances in neural information processing systems*, 29, 2016.

Sarkar, R. Low distortion delaunay embedding of trees in hyperbolic plane. In *International symposium on graph drawing*, pp. 355–366. Springer, 2011.

Shen, X., Dai, Q., Chung, F.-I., Lu, W., and Choi, K.-S. Adversarial deep network embedding for cross-network node classification. In *Proceedings of the AAAI conference on artificial intelligence*, volume 34, pp. 2991–2999, 2020.

Shervashidze, N., Schweitzer, P., Van Leeuwen, E. J., Mehlhorn, K., and Borgwardt, K. M. Weisfeiler-lehman graph kernels. *The Journal of Machine Learning Research.*, 12(9), 2011.

Singhal, P., Walambe, R., Ramanna, S., and Kotecha, K. Domain adaptation: challenges, methods, datasets, and applications. *IEEE access*, 11:6973–7020, 2023.

Strogatz, S. H. *Nonlinear dynamics and chaos: with applications to physics, biology, chemistry, and engineering (studies in nonlinearity)*, volume 1. Westview press, 2001.

Sun, K., Zhu, Z., and Lin, Z. Adagcn: Adaboosting graph convolutional networks into deep models. In *International Conference on Learning Representations*, 2020.

Sun, L., Ye, J., Peng, H., Wang, F., and Yu, P. S. Self-supervised continual graph learning in adaptive riemannian spaces. In *Proceedings of the AAAI Conference on Artificial Intelligence*, volume 37, pp. 4633–4642, 2023.

Sun, L., Huang, Z., Wang, Z., Wang, F., Peng, H., and Yu, P. S. Motif-aware riemannian graph neural network with generative-contrastive learning. In *Proceedings of the AAAI Conference on Artificial Intelligence*, volume 38, pp. 9044–9052, 2024.

Sun, L., Zhou, S., Fang, B., Zhang, H., Ye, J., Ye, Y., and Yu, P. S. Trace: Structural riemannian bridge matching for transferable source localization in information propagation. In *Proceedings of IJCAI*, 2025.

Sutherland, J. J., O'brien, L. A., and Weaver, D. F. Spline-fitting with a genetic algorithm: A method for developing classification structure- activity relationships. *Journal of chemical information and computer sciences*, 43(6): 1906–1915, 2003.

Tifrea, A., Bécigneul, G., and Ganea, O.-E. Poincaré glove: Hyperbolic word embeddings. *arXiv preprint arXiv:1810.06546*, 2018.

Tong, A., Malkin, N., Huguet, G., Zhang, Y., Rector-Brooks, J., Fatras, K., Wolf, G., and Bengio, Y. Conditional flow matching: Simulation-free dynamic optimal transport. *arXiv preprint arXiv:2302.00482*, 2(3), 2023.

Wale, N., Watson, I. A., and Karypis, G. Comparison of descriptor spaces for chemical compound retrieval and classification. *Knowledge and Information Systems*, 14: 347–375, 2008.

Wang, J., Guo, J., Sun, Y., Gao, J., Wang, S., Yang, Y., and Yin, B. Dggn: Decoupled graph neural networks with structural consistency between attribute and graph embedding representations. *IEEE Transactions on Big Data*, 2024a.

Wang, Y., Wang, M., Su, H., Yin, N., Yao, Q., and Kwok, J. Degree-conscious spiking graph for cross-domain adaptation. *arXiv preprint arXiv:2410.06883*, 2024b.

Wang, Y., Zhang, S., Ye, J., Peng, H., and Sun, L. A mixed-curvature graph diffusion model. In *Proceedings of the International Conference on Information and Knowledge Management*, pp. 2482–2492, 2024c.

Wang, Y., Wang, M., Huang, Z., Liu, S., and Yin, N. Nested graph pseudo-label refinement for noisy label domain adaptation learning. *arXiv preprint arXiv:2508.00716*, 2025a.

Wang, Y., Yin, N., Xiao, M., Yi, X., Liu, S., and Liang, S. Dusego: Dual second-order equivariant graph ordinary differential equation. *ACM Transactions on Knowledge Discovery from Data*, 20(1):1–18, 2025b.

Wu, M., Pan, S., Zhou, C., Chang, X., and Zhu, X. Unsupervised domain adaptive graph convolutional networks. In *Proceedings of the ACM Web Conference*, pp. 1457–1467, 2020.

Wu, M., Zheng, X., Zhang, Q., Shen, X., Luo, X., Zhu, X., and Pan, S. Graph learning under distribution shifts: A comprehensive survey on domain adaptation, out-of-distribution, and continual learning. *arXiv preprint arXiv:2402.16374*, 2024.

Xu, K., Hu, W., Leskovec, J., and Jegelka, S. How powerful are graph neural networks? *arXiv preprint arXiv:1810.00826*, 2018.

Xu, Y., Cao, H., Xie, L., Li, X.-L., Chen, Z., and Yang, J. Video unsupervised domain adaptation with deep learning: A comprehensive survey. *ACM Computing Surveys*, 56(12):1–36, 2024.

Yin, N., Shen, L., Li, B., Wang, M., Luo, X., Chen, C., Luo, Z., and Hua, X.-S. Deal: An unsupervised domain adaptive framework for graph-level classification. In *Proceedings of the ACM International Conference on Multimedia*, pp. 3470–3479, 2022.

Yin, N., Shen, L., Wang, M., Liu, X., Chen, C., and Hua, X.-S. Dream: A dual variational framework for unsupervised graph domain adaptation. *IEEE Transactions on Pattern Analysis and Machine Intelligence*, 47(11):10787–10800, 2025a. doi: 10.1109/TPAMI.2025.3596054.

Yin, N., Shen, L., Wang, M., Liu, X., Chen, C., and Hua, X.-S. Dream: a dual variational framework for unsupervised graph domain adaptation. *IEEE Transactions on Pattern Analysis and Machine Intelligence*, 2025b.

Zagheni, O., Eijkelboom, F., Pouplin, A., and Bekkers, E. J. Towards variational flow matching on general geometries. *arXiv preprint arXiv:2502.12981*, 2025.

Zhang, Z., Wang, J., and Zha, H. Adaptive manifold learning. *IEEE transactions on pattern analysis and machine intelligence*, 34(2):253–265, 2011.

Zou, Y., Yu, Z., Kumar, B., and Wang, J. Unsupervised domain adaptation for semantic segmentation via class-balanced self-training. In *Proceedings of the European Conference on Computer Vision.*, pp. 289–305, 2018.

Appendix

A. Riemannian Geometry and Stereographic Model

Let \mathcal{M}_c denote the d -dimensional Riemannian manifold with constant curvature c , defined as the interior of a ball $\mathcal{M}_c = \{x \in \mathbb{R}^d : -c\|x\|^2 < 1\}$. The Riemannian metric tensor g_x^c is conformally equivalent to the Euclidean metric g_x^E , given by $g_x^c = (\lambda_x^c)^2 g_x^E$, where the conformal factor is $\lambda_x^c = 2/(1 + c\|x\|^2)$. The curvature c determines the geometry: $c < 0$ for the Hyperbolic space \mathbb{H}^d , $c > 0$ for the Spherical space \mathbb{S}^d , and $c \rightarrow 0$ for the Euclidean space \mathbb{E}^d .

Exponential and Logarithmic Maps. Transformations between the manifold \mathcal{M}_c and the tangent space $T_x \mathcal{M}_c$ (isomorphic to \mathbb{R}^d) are mediated by the Exponential map $\text{Exp}_x^c : T_x \mathcal{M}_c \rightarrow \mathcal{M}_c$ and the Logarithmic map $\text{Log}_x^c : \mathcal{M}_c \rightarrow T_x \mathcal{M}_c$. For the origin 0, these maps are:

$$\text{Exp}_0^c(v) = \tan_c(\|v\|) \frac{v}{\|v\|}, \quad \text{Log}_0^c(y) = \tan_c^{-1}(\|y\|) \frac{y}{\|y\|},$$

where $\tan_c(\cdot)$ and $\tan_c^{-1}(\cdot)$ are curvature-dependent trigonometric functions (e.g., $\tanh / \text{arctanh}$ for $c < 0$).

Geodesics and Distance. Geodesics generalize the concept of straight lines to Riemannian manifolds, representing the locally length-minimizing curves. The unique geodesic segment $\gamma : [0, 1] \rightarrow \mathcal{M}_c$ connecting a source point x to a target point y is parameterized as: $\gamma(t) = \text{Exp}_x^c(t \cdot \text{Log}_x^c(y))$. The Riemannian distance $d_{\mathcal{M}}(x, y)$ is the length of this geodesic, calculated as $d_{\mathcal{M}}(x, y) = \|\text{Log}_x^c(y)\|_x$.

Parallel Transport. Comparing tangent vectors at distinct points requires Parallel Transport. The transport of a vector $v \in T_0 \mathcal{M}_c$ to $T_x \mathcal{M}_c$ along the geodesic connecting 0 and x is given by $P_{0 \rightarrow x}(v) = (\lambda_0^c / \lambda_x^c)v$. This operator ensures that the geometric properties of feature vectors (e.g., orientation) are preserved during transport.

Riemannian Polar Coordinates. Formally, any point $x \in \mathcal{M}_c \setminus \{0\}$ can be uniquely represented via the polar decomposition of its tangent vector in $T_0 \mathcal{M}_c$. We define the radial coordinate r_x and angular coordinate u_x as:

$$r_x = \|\text{Log}_0^c(x)\|_2, \quad u_x = \frac{\text{Log}_0^c(x)}{\|\text{Log}_0^c(x)\|_2}.$$

Mathematically, r_x corresponds to the Riemannian geodesic distance from the origin, i.e., $r_x = d_{\mathcal{M}}(0, x)$, while $u_x \in \mathbb{S}^{d-1}$ represents the direction in the tangent space.

B. Proof of Proposition 4.1

In this section, we provide the detailed derivation for the volume growth behavior of geodesic balls in spaces with constant sectional curvature, specifically proving the claims in Proposition 4.1 regarding Euclidean (\mathbb{E}), Spherical (\mathbb{S}), and Hyperbolic (\mathbb{H}) geometries.

Let \mathcal{M}_κ^d be a d -dimensional simply connected Riemannian manifold with constant sectional curvature κ . In the geodesic polar coordinates (r, Θ) around a reference point (origin) $\mathbf{o} \in \mathcal{M}_\kappa^d$, where $r \in [0, R]$ is the radial distance and $\Theta \in \mathbb{S}^{d-1}$ is the angular coordinate, the Riemannian metric tensor g is given by:

$$ds^2 = dr^2 + S_\kappa^2(r) d\Theta^2, \quad (6)$$

where $d\Theta^2$ denotes the standard metric on the unit sphere \mathbb{S}^{d-1} , and $S_\kappa(r)$ is the generalized sine function (or warping function) determined by the curvature κ :

$$S_\kappa(r) = \begin{cases} \frac{1}{\sqrt{\kappa}} \sin(\sqrt{\kappa}r) & \text{if } \kappa > 0 \quad (\mathbb{S}), \\ r & \text{if } \kappa = 0 \quad (\mathbb{E}), \\ \frac{1}{\sqrt{|\kappa|}} \sinh(\sqrt{|\kappa|}r) & \text{if } \kappa < 0 \quad (\mathbb{H}). \end{cases} \quad (7)$$

The volume of a geodesic ball $\mathcal{B}(R)$ of radius R is obtained by integrating the volume element $dV = \sqrt{\det g} dr d\Theta$ over the ball. The determinant of the metric is given by $\sqrt{\det g} = S_\kappa(r)^{d-1} \sqrt{\det g_{\mathbb{S}^{d-1}}}$. Thus, the volume is:

$$\text{Vol}(\mathcal{B}_\mathcal{M}(R)) = \int_{\mathbb{S}^{d-1}} d\Theta \int_0^R S_\kappa(r)^{d-1} dr = \Omega_{d-1} \int_0^R S_\kappa(r)^{d-1} dr, \quad (8)$$

where $\Omega_{d-1} = \frac{2\pi^{d/2}}{\Gamma(d/2)}$ is the surface area of the unit sphere S^{d-1} .

Case 1: Euclidean Space ($\mathbb{E}, \kappa = 0$) For Euclidean space, $S_0(r) = r$. Substituting this into Eq. (8):

$$\text{Vol}(\mathcal{B}_{\mathbb{E}}(R)) = \Omega_{d-1} \int_0^R r^{d-1} dr = \Omega_{d-1} \left[\frac{r^d}{d} \right]_0^R = \frac{\Omega_{d-1}}{d} R^d. \quad (9)$$

The volume grows polynomially with respect to the radius R , i.e., $\text{Vol}(\mathcal{B}_{\mathbb{E}}(R)) \propto R^d$.

Case 2: Spherical Space ($\mathbb{S}, \kappa = c > 0$) For Spherical space, $S_c(r) = \frac{1}{\sqrt{c}} \sin(\sqrt{c}r)$. The volume integral becomes:

$$\text{Vol}(\mathcal{B}_{\mathbb{S}}(R)) = \Omega_{d-1} \int_0^R \left(\frac{\sin(\sqrt{c}r)}{\sqrt{c}} \right)^{d-1} dr. \quad (10)$$

Since $|\sin(\cdot)| \leq 1$, the integrand is bounded. Moreover, the space is compact (a closed manifold) with a maximum diameter of π/\sqrt{c} . Thus, for any R , the volume is strictly bounded from above by the total volume of the sphere. As R increases (periodically wrapping around the sphere), the volume remains finite and does not diverge to infinity.

Case 3: Hyperbolic Space ($\mathbb{H}, \kappa = -|c| < 0$) For Hyperbolic space, $S_{-|c|}(r) = \frac{1}{\sqrt{|c|}} \sinh(\sqrt{|c|}r)$. The volume integral is:

$$\text{Vol}(\mathcal{B}_{\mathbb{H}}(R)) = \frac{\Omega_{d-1}}{(\sqrt{|c|})^{d-1}} \int_0^R \sinh^{d-1}(\sqrt{|c|}r) dr. \quad (11)$$

We analyze the asymptotic behavior as $R \rightarrow \infty$. Recall that $\sinh(x) = \frac{e^x - e^{-x}}{2}$. For large x , $\sinh(x) \sim \frac{1}{2}e^x$. Therefore, the integrand behaves as:

$$\sinh^{d-1}(\sqrt{|c|}r) \sim \left(\frac{e^{\sqrt{|c|}r}}{2} \right)^{d-1} = \frac{1}{2^{d-1}} e^{(d-1)\sqrt{|c|}r}. \quad (12)$$

Substituting this asymptotic form into the integral:

$$\begin{aligned} \text{Vol}(\mathcal{B}_{\mathbb{H}}(R)) &\approx \frac{\Omega_{d-1}}{(\sqrt{|c|})^{d-1} 2^{d-1}} \int_0^R e^{(d-1)\sqrt{|c|}r} dr \\ &= \frac{\Omega_{d-1}}{(2\sqrt{|c|})^{d-1}} \left[\frac{e^{(d-1)\sqrt{|c|}r}}{(d-1)\sqrt{|c|}} \right]_0^R \\ &\approx \frac{\Omega_{d-1}}{(d-1)|c|^{d/2} 2^{d-1}} e^{(d-1)\sqrt{|c|}R}. \end{aligned} \quad (13)$$

Finally, taking the limit of the ratio:

$$\lim_{R \rightarrow \infty} \frac{\text{Vol}(\mathcal{B}_{\mathbb{H}}(R))}{\exp((d-1)\sqrt{|c|}R)} = \frac{\Omega_{d-1}}{(d-1)|c|^{d/2} 2^{d-1}} = \text{const} > 0. \quad (14)$$

This confirms that the volume in hyperbolic space undergoes exponential expansion with respect to the radius R , concluding the proof. \square

C. Proof of Theorem 4.2

In this section, we utilize the properties of the Riemannian metric tensor in polar coordinates to prove the orthogonality of the structural and semantic gradient flows, and we derive the scaling law of the available semantic capacity in hyperbolic space.

Consider a d -dimensional Riemannian manifold \mathcal{M}_c with constant sectional curvature $-c$ (where $c > 0$). We adopt the geodesic polar coordinate system $\mathbf{z} = (r, \Theta)$, where $r \in \mathbb{R}^+$ is the radial distance from the origin (representing hierarchy/structure) and $\Theta \in \mathcal{S}^{d-1}$ contains the $d-1$ angular coordinates (representing semantics).

In this coordinate system, the Riemannian metric tensor G decomposes into a block-diagonal form (a warped product structure):

$$G(r, \Theta) = \begin{pmatrix} 1 & \mathbf{0}^\top \\ \mathbf{0} & S_c^2(r)g_{\mathcal{S}^{d-1}}(\Theta) \end{pmatrix}, \quad (15)$$

where $g_{\mathcal{S}^{d-1}}$ is the standard metric on the unit sphere, and $S_c(r)$ is the warping function defined as:

$$S_c(r) = \frac{1}{\sqrt{c}} \sinh(\sqrt{c}r). \quad (16)$$

Definition of Gradient Flows. Let $\mathcal{L}(r, \Theta)$ be the objective function. The Riemannian gradient $\nabla_G \mathcal{L}$ is related to the Euclidean gradient $\nabla_E \mathcal{L} = (\frac{\partial \mathcal{L}}{\partial r}, \frac{\partial \mathcal{L}}{\partial \Theta})^\top$ by the inverse metric tensor:

$$\nabla_G \mathcal{L} = G^{-1} \nabla_E \mathcal{L} = \begin{pmatrix} 1 & \mathbf{0}^\top \\ \mathbf{0} & S_c^{-2}(r)g_{\mathcal{S}^{d-1}}^{-1} \end{pmatrix} \begin{pmatrix} \frac{\partial \mathcal{L}}{\partial r} \\ \frac{\partial \mathcal{L}}{\partial \Theta} \end{pmatrix}. \quad (17)$$

We define the structural gradient flow ($\nabla_r \mathcal{L}$) and semantic gradient flow ($\nabla_\theta \mathcal{L}$) as the projections of the full Riemannian gradient onto the radial and angular tangent subspaces, respectively:

$$\nabla_r \mathcal{L} = \left(\frac{\partial \mathcal{L}}{\partial r} \right) \mathbf{e}_r, \quad (18)$$

$$\nabla_\theta \mathcal{L} = \left(S_c^{-2}(r)g_{\mathcal{S}^{d-1}}^{-1} \frac{\partial \mathcal{L}}{\partial \Theta} \right) \cdot \mathbf{e}_\Theta, \quad (19)$$

where \mathbf{e}_r and \mathbf{e}_Θ represent the basis vectors for the radial and angular components.

Orthogonality Check. We compute the inner product of these two vectors under the Riemannian metric G :

$$\langle \nabla_r \mathcal{L}, \nabla_\theta \mathcal{L} \rangle_G = (\nabla_r \mathcal{L})^\top G (\nabla_\theta \mathcal{L}). \quad (20)$$

Substituting the block-diagonal form of G :

$$\langle \nabla_r \mathcal{L}, \nabla_\theta \mathcal{L} \rangle_G = \left(\frac{\partial \mathcal{L}}{\partial r} \quad \mathbf{0}^\top \right) \begin{pmatrix} 1 & \mathbf{0}^\top \\ \mathbf{0} & S_c^2(r)g_{\mathcal{S}^{d-1}} \end{pmatrix} \begin{pmatrix} \mathbf{0} \\ \nabla_\theta \mathcal{L} \end{pmatrix} = 0. \quad (21)$$

The cross-terms vanish strictly because the off-diagonal blocks of the metric tensor are zero in the polar coordinate system. This proves that optimizing the semantic alignment (changing Θ) incurs zero projection onto the structural dimension (r), ensuring theoretically perfect disentanglement.

The “available semantic capacity” at a hierarchical depth r corresponds to the geometric volume (or area) of the geodesic sphere \mathcal{S}_r^{d-1} embedded in the hyperbolic space at radius r .

The induced metric on the shell at radius r is $H_r = S_c^2(r)g_{\mathcal{S}^{d-1}}$. The volume element is given by:

$$d\text{Vol}_r = \sqrt{\det(H_r)} d\Theta = S_c(r)^{d-1} \sqrt{\det(g_{\mathcal{S}^{d-1}})} d\Theta. \quad (22)$$

Integrating over the full angular space Θ :

$$\text{Capacity}(r) = \text{Vol}(\mathcal{S}_r^{d-1}) = \int_{\mathcal{S}^{d-1}} S_c(r)^{d-1} d\text{Vol}_{\mathcal{S}^{d-1}} = \Omega_{d-1} S_c(r)^{d-1}, \quad (23)$$

where Ω_{d-1} is the area of the unit Euclidean sphere. Substituting the hyperbolic warping function $S_c(r) = \frac{1}{\sqrt{c}} \sinh(\sqrt{c}r)$:

$$\text{Capacity}(r) \propto \sinh^{d-1}(\sqrt{c}r). \quad (24)$$

For large r (deep in the hierarchy), $\sinh(x) \approx \frac{1}{2}e^x$. Thus:

$$\text{Capacity}(r) \propto \left(e^{\sqrt{c}r}\right)^{d-1} = e^{(d-1)\sqrt{c}r}. \quad (25)$$

This confirms that the available semantic space expands exponentially with the radius r , validating the scaling law stated in the theorem. \square

D. Proof of Theorem 4.3

In this section, we provide the stability analysis of the adversarial training dynamics. We prove that under the condition where interaction terms dominate local curvature, the system's equilibrium exhibits spectral instability, characterized by purely imaginary eigenvalues.

Consider the standard adversarial domain adaptation objective as a zero-sum minimax game between the feature generator $\theta \in \mathbb{R}^n$ and the domain discriminator $\phi \in \mathbb{R}^m$:

$$\min_{\theta} \max_{\phi} \mathcal{L}_{adv}(\theta, \phi). \quad (26)$$

The continuous-time optimization dynamics are governed by the gradient vector field $v(\omega)$, where $\omega = (\theta, \phi)$ represents the joint parameter state:

$$v(\omega) = \begin{pmatrix} \nabla_{\theta} \mathcal{L}_{adv}(\theta, \phi) \\ -\nabla_{\phi} \mathcal{L}_{adv}(\theta, \phi) \end{pmatrix}. \quad (27)$$

A local Nash equilibrium $\omega^* = (\theta^*, \phi^*)$ is defined as a stationary point of this vector field, satisfying $v(\omega^*) = \mathbf{0}$.

To analyze the local stability properties, we examine the Jacobian matrix $J(\omega)$ of the vector field $v(\omega)$ evaluated at the equilibrium ω^* . The Jacobian captures the first-order linearization of the dynamics and is composed of the block Hessian matrices:

$$J(\omega^*) = \nabla v(\omega^*) = \begin{pmatrix} \nabla_{\theta\theta}^2 \mathcal{L}_{adv} & \nabla_{\theta\phi}^2 \mathcal{L}_{adv} \\ -\nabla_{\phi\theta}^2 \mathcal{L}_{adv} & -\nabla_{\phi\phi}^2 \mathcal{L}_{adv} \end{pmatrix} \Big|_{\omega^*}. \quad (28)$$

Let us define the block matrices for notation simplicity:

- $H_{\theta\theta} = \nabla_{\theta\theta}^2 \mathcal{L}_{adv}$ and $H_{\phi\phi} = -\nabla_{\phi\phi}^2 \mathcal{L}_{adv}$ represent the local curvature (self-interaction) terms.
- $K = \nabla_{\theta\phi}^2 \mathcal{L}_{adv}$ represents the interaction term between the generator and discriminator. Note that $\nabla_{\phi\theta}^2 \mathcal{L}_{adv} = K^\top$.

Substituting these terms, the Jacobian matrix becomes:

$$J = \begin{pmatrix} H_{\theta\theta} & K \\ -K^\top & H_{\phi\phi} \end{pmatrix}. \quad (29)$$

The condition that “local curvature is dominated by the interaction term” implies that the magnitudes of the self-curvature terms are negligible compared to the cross-terms. Mathematically, we assume the limit case where $H_{\theta\theta} \approx \mathbf{0}$ and $H_{\phi\phi} \approx \mathbf{0}$. This simplifies the Jacobian to a Hamiltonian matrix structure:

$$J_{dom} = \begin{pmatrix} \mathbf{0} & K \\ -K^\top & \mathbf{0} \end{pmatrix}. \quad (30)$$

We now solve for the eigenvalues λ of J_{dom} . Let $\mathbf{x} = (\mathbf{u}, \mathbf{v})$ be a non-zero eigenvector corresponding to eigenvalue λ , such that $J_{dom}\mathbf{x} = \lambda\mathbf{x}$. This yields the coupled system:

$$K\mathbf{v} = \lambda\mathbf{u}, \quad (31)$$

$$-K^\top \mathbf{u} = \lambda\mathbf{v}. \quad (32)$$

Multiplying Eq. (31) by λ and substituting Eq. (32), we obtain:

$$\lambda^2 \mathbf{u} = \lambda(K\mathbf{v}) = K(\lambda\mathbf{v}) = K(-K^\top \mathbf{u}) = -(KK^\top)\mathbf{u}. \quad (33)$$

This equation implies that λ^2 is an eigenvalue of the matrix $M = -KK^\top$.

Since K is a real matrix, the product KK^\top is symmetric and positive semi-definite. Let $\sigma^2 \geq 0$ denote an eigenvalue of KK^\top (where σ corresponds to a singular value of K). Then, the eigenvalues of M are real and non-positive ($-\sigma^2$). Consequently, the eigenvalues of the Jacobian J_{dom} are given by:

$$\lambda = \pm i\sigma. \quad (34)$$

The eigenvalues are purely imaginary ($\text{Re}(\lambda) = 0, \text{Im}(\lambda) \neq 0$ for $\sigma > 0$). In dynamical systems theory, a fixed point with purely imaginary eigenvalues is classified as a center. Trajectories in the vicinity of a center do not converge asymptotically but instead form closed orbits (limit cycles). This theoretically confirms the oscillatory nature and instability of standard adversarial training when interaction terms dominate. \square

E. Proof of Theorem 4.4

In this section, we analyze the global convergence properties of the DisRFM optimization process. We show that unlike the vector field of adversarial games which contains rotational components (leading to limit cycles), the dynamics of Flow Matching are governed by a conservative gradient field, ensuring asymptotic stability.

Let $\theta \in \mathbb{R}^p$ denote the parameters of the vector field network v_θ . The training objective for Flow Matching is the regression loss:

$$\mathcal{L}_{FM}(\theta) = \mathbb{E}_{t, \mathbf{z}_S, \mathbf{z}_T} [\|v_\theta(\mathbf{z}_t, t) - \mathbf{u}_t(\mathbf{z}_t)\|^2]. \quad (35)$$

In the continuous-time limit (as the learning rate $\eta \rightarrow 0$), the optimization trajectory $\theta(t)$ generated by Stochastic Gradient Descent (SGD) follows the Gradient Flow differential equation:

$$\frac{d\theta(t)}{dt} = -\nabla_\theta \mathcal{L}_{FM}(\theta(t)). \quad (36)$$

To prove stability, we propose the loss function $\mathcal{L}_{FM}(\theta)$ itself as a candidate Lyapunov function $V(\theta)$. A valid strict Lyapunov function must satisfy two conditions:

1. **Positive Definiteness:** $V(\theta) \geq 0$ (bounded from below), which holds trivially since \mathcal{L}_{FM} is a squared norm.
2. **Negative Orbital Derivative:** The time derivative $\dot{V}(\theta)$ along the system trajectories must be strictly non-positive.

We compute the time derivative of the objective function along the optimization path using the Chain Rule:

$$\frac{d}{dt} \mathcal{L}_{FM}(\theta(t)) = \left\langle \nabla_\theta \mathcal{L}_{FM}(\theta(t)), \frac{d\theta(t)}{dt} \right\rangle. \quad (37)$$

Substituting the dynamics from Eq. (36):

$$\begin{aligned} \frac{d}{dt} \mathcal{L}_{FM}(\theta(t)) &= \langle \nabla_\theta \mathcal{L}_{FM}(\theta), -\nabla_\theta \mathcal{L}_{FM}(\theta) \rangle \\ &= -\|\nabla_\theta \mathcal{L}_{FM}(\theta)\|^2. \end{aligned} \quad (38)$$

From this derivation, we observe:

- **Monotonicity:** Since the squared norm $\|\cdot\|^2$ is non-negative, the derivative is strictly non-positive:

$$\frac{d}{dt} \mathcal{L}_{FM}(\theta(t)) \leq 0. \quad (39)$$

This implies that the “energy” (loss) of the system decreases monotonically over time.

- **Stationarity:** The derivative is zero ($\frac{d}{dt}\mathcal{L}_{FM} = 0$) if and only if $\|\nabla_{\theta}\mathcal{L}_{FM}\| = 0$, which corresponds to the critical points (stationary points) of the loss landscape.

In dynamical systems, a vector field \mathbf{F} is conservative if it can be expressed as the gradient of a scalar potential, i.e., $\mathbf{F} = -\nabla\Phi$.

- **DisRFM:** The update field is $\mathbf{F}_{FM} = -\nabla\mathcal{L}_{FM}$. It is strictly conservative. The system cannot return to a previous state with higher energy, thereby structurally precluding closed orbits (limit cycles).
- **Adversarial Baselines:** The update field involves a rotational component (curl) due to the minimax structure ($\mathbf{F}_{Adv} = (\nabla_{\theta}\mathcal{L}, -\nabla_{\phi}\mathcal{L})$). It is generally non-conservative, allowing energy to oscillate indefinitely.

Therefore, according to LaSalle's Invariance Principle (Khalil & Grizzle, 2002), the trajectory $\theta(t)$ of DisRFM is guaranteed to converge asymptotically to the set of stationary points where $\nabla_{\theta}\mathcal{L}_{FM} = 0$. \square

F. Proof of Theorem 4.5

In this section, we provide the derivation for the tighter generalization bound achieved by DisRFM. We rely on the seminal domain adaptation theory by Ben-David et al. (Ben-David et al., 2010) and decompose the realized divergence term into geometric and optimization components to demonstrate the superiority of our framework.

Let \mathcal{H} be a hypothesis space. For any hypothesis $h \in \mathcal{H}$, let $\epsilon_S(h)$ and $\epsilon_T(h)$ be the risks on the source and target domains, respectively. The standard bound is given by:

$$\epsilon_T(h) \leq \epsilon_S(h) + \frac{1}{2}\hat{d}_{\mathcal{H}\Delta\mathcal{H}}(\mathcal{D}_S, \mathcal{D}_T) + C, \quad (40)$$

where $\hat{d}_{\mathcal{H}\Delta\mathcal{H}}$ is the empirical divergence between the source and target feature distributions learned by the model. A lower $\hat{d}_{\mathcal{H}\Delta\mathcal{H}}$ implies better alignment and, consequently, a tighter bound on the target risk.

We posit that the realized divergence \hat{d} achieved by a model is not solely determined by the domain data but is limited by the model's ability to represent and align the data. It can be decomposed as:

$$\hat{d}_{\text{realized}} = d_{\text{optimal}} + \underbrace{\text{Err}_{\text{geo}}}_{\text{Distortion}} + \underbrace{\text{Err}_{\text{opt}}}_{\text{Convergence Gap}}, \quad (41)$$

where d_{optimal} is the intrinsic divergence between domains, Err_{geo} is the error caused by the geometric embedding space, and Err_{opt} is the residual error due to imperfect optimization.

Standard domain adaptation methods embed graph data into Euclidean space \mathbb{E}^d . However, graph datasets (especially those in DisRFM) often exhibit latent hierarchical structures. According to Sarkar's construction (Sarkar, 2011), embedding a tree-like hierarchy with n nodes into a d -dimensional Euclidean space incurs a geometric distortion that scales as:

$$\text{Err}_{\text{geo}}^{\text{Base}} = \Omega(n^{1/d}). \quad (42)$$

This distortion corrupts the structural information of the graph features, preventing the alignment module from correctly matching structurally similar nodes across domains, thereby inflating the realized divergence.

DisRFM operates in the Riemannian polar space, which includes a Hyperbolic component \mathbb{H} . As shown in Proposition 4.1, hyperbolic space has exponential capacity matching the growth of hierarchies. Consequently, it can embed tree structures with arbitrarily low distortion:

$$\text{Err}_{\text{geo}}^{\text{DisRFM}} \approx 0. \quad (43)$$

The improvement in the bound due to geometry is thus:

$$\Delta_{\text{geo}} = \text{Err}_{\text{geo}}^{\text{Base}} - \text{Err}_{\text{geo}}^{\text{DisRFM}} = \Omega(n^{1/d}). \quad (44)$$

Adversarial methods (e.g., DANN (Ajakan et al., 2014), CDAN (Long et al., 2018)) rely on a minimax game $\min_{\theta} \max_{\phi} \mathcal{L}_{adv}$. As proven in Theorem 4.3, the equilibrium of this game often exhibits pure imaginary eigenvalues, leading to limit cycles

(oscillations) rather than convergence to the global minimum. The optimization typically halts at a non-optimal stationary point or fluctuates around it, leaving a positive residual gap:

$$\text{Err}_{\text{opt}}^{\text{Base}} = \xi_{\text{opt}} > 0. \quad (45)$$

DisRFM utilizes Flow Matching with a conservative gradient field. As proven in Theorem 4.4, the objective \mathcal{L}_{FM} acts as a Lyapunov function, guaranteeing asymptotic convergence to the stationary set. Empirically and theoretically, regression-based flow matching allows the model to reach a lower minimum of the divergence objective:

$$\text{Err}_{\text{opt}}^{\text{DisRFM}} \approx 0 \quad (\text{or } \ll \xi_{\text{opt}}). \quad (46)$$

The improvement in the bound due to optimization is:

$$\Delta_{\text{opt}} = \text{Err}_{\text{opt}}^{\text{Base}} - \text{Err}_{\text{opt}}^{\text{DisRFM}} \approx \xi_{\text{opt}}. \quad (47)$$

Combining the results above, we compare the realized divergence of DisRFM against the baseline:

$$\hat{d}_{\text{DisRFM}} = d_{\text{optimal}} + 0 + 0, \quad (48)$$

$$\hat{d}_{\text{Base}} = d_{\text{optimal}} + \Omega(n^{1/d}) + \xi_{\text{opt}}. \quad (49)$$

Subtracting the two yields the claimed inequality:

$$\hat{d}_{\text{DisRFM}} \leq \hat{d}_{\text{Base}} - \Omega(n^{1/d}) - \xi_{\text{opt}}. \quad (50)$$

Substituting this back into Ben-David's theorem proves that DisRFM achieves a strictly tighter upper bound on the target risk $\epsilon_T(h)$. \square

G. Dataset

G.1. Dataset Description

Table 3. Statistics of the experimental datasets.

Datasets	Graphs	Avg. Nodes	Avg. Edges	Classes
NCI1	4,110	29.87	32.30	2
MUTAGENICITY	4,337	30.32	30.77	2
PROTEINS	1,113	39.1	72.8	2
ogbg-molhiv	41,127	25.5	27.5	2
DD	1,178	284.32	715.66	2
COX2	467	41.22	43.45	2
COX2_MD	303	26.28	335.12	2
BZR	405	35.75	38.36	2
BZR_MD	306	21.30	225.06	2

We conduct extensive experiments on a variety of datasets. The statistics of the datasets are summarized in Table 3. More detailed descriptions of each dataset are provided as follows:

- For structure-based domain shifts:

– **PROTEINS.** The PROTEINS dataset (Dobson & Doig, 2003) consists of 1,113 protein graphs, each annotated with a binary label indicating whether the protein is an enzyme. In each graph, nodes correspond to amino acids, and edges connect amino acids that are within 6 Å of each other along the sequence. We further partition the dataset into four subsets, denoted as P0, P1, P2, and P3, according to edge density and node density.

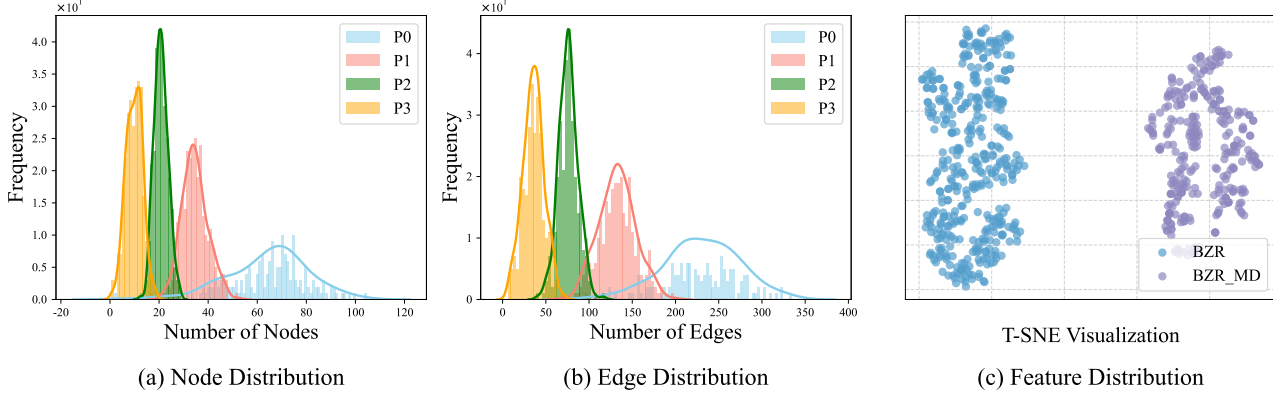


Figure 5. Visualization of domain shifts across different types. (a) Node distribution shift between sub-datasets of PROTEINS. (b) Edge distribution shift between sub-datasets of PROTEINS. (c) Feature distribution shift between BZR and BZR_MD datasets.

- **NCI1.** The NCI1 dataset (Wale et al., 2008) consists of 4,100 molecular graphs, where nodes represent atoms and edges correspond to chemical bonds. Each graph is annotated with a binary label indicating whether the molecule inhibits cancer cell growth. We further partition the dataset into four subsets, denoted as N0, N1, N2, and N3, according to edge density and node density.
- **MUTAGENICITY.** The MUTAGENICITY dataset (Kazius et al., 2005) consists of 4,337 molecular graphs, where nodes represent atoms and edges correspond to chemical bonds. Each graph is annotated with a binary label indicating whether the compound is mutagenic. Following the PROTEINS dataset, we further partition the dataset into four subsets, denoted as M0, M1, M2, and M3, according to edge density and node density.
- **ogbg-molhiv.** The ogbg-molhiv dataset (Hu et al., 2021) consists of 41,127 molecular graphs, where nodes represent atoms and edges correspond to chemical bonds. Each graph is annotated with a binary label indicating whether the molecule exhibits HIV inhibitory activity. Following the PROTEINS dataset, we further partition the dataset into four subsets, denoted as H0, H1, H2, and H3, according to edge density and node density.
- For feature-based domain shifts:
 - **DD.** The DD dataset (Dobson & Doig, 2003) consists of 1,178 protein structure graphs, where nodes correspond to amino acids and edges encode spatial or chemical proximity between them. Compared to the PROTEINS dataset, DD graphs are substantially larger and denser, thereby introducing pronounced structural variability while preserving similar semantic labels.
 - **COX2.** The COX2 dataset (Sutherland et al., 2003) consists of 467 molecular graphs, while COX2_MD contains 303 modified molecular graphs. In both datasets, nodes correspond to atoms and edges represent chemical bonds. COX2_MD introduces controlled structural variations to COX2 while preserving semantic labels.
 - **BZR.** The BZR dataset (Sutherland et al., 2003) consists of 405 molecular graphs, while BZR_MD contains 306 structurally modified graphs derived from BZR. In both datasets, nodes correspond to atoms and edges represent chemical bonds. BZR_MD introduces controlled structural variations to simulate domain shifts while preserving consistent label semantics.

G.2. Data Processing

For datasets from the TUDataset¹ (e.g., PROTEINS and NCI1), we adopt the standard preprocessing and normalization procedures provided by PyTorch Geometric². For datasets from the Open Graph Benchmark (OGB)³, such as ogbg-molhiv, we follow the official OGB preprocessing and normalization protocols.

H. Baselines

In this part, we introduce the details of the compared baselines as follows:

¹<https://chrsmrrs.github.io/datasets/>

²<https://pyg.org/>

³<https://ogb.stanford.edu/>

- **Graph kernel method.** We compare DisRFM with two graph kernel methods:
 - **WL subtree:** WL subtree (Shervashidze et al., 2011) is a graph kernel method that computes graph similarity via a kernel function, encoding local neighborhood structures into subtree patterns and efficiently capturing topological information within graphs.
 - **PathNN:** PathNN (Michel et al., 2023) is an expressive graph neural network that models graphs by aggregating information along simple paths, enabling accurate capture of long-range dependencies and higher-order structural patterns beyond local neighborhoods.
- **General Graph Geural Networks.** We compare DisRFM with four general graph neural networks:
 - **GCN:** GCN (Kipf & Welling, 2017) is a message-passing graph neural network that updates node representations by aggregating and normalizing features from immediate neighbors, effectively capturing local structural and attribute information in graphs.
 - **GIN:** GIN (Xu et al., 2018) is a graph neural network with an injective aggregation function that sums neighbor features, achieving strong expressive power equivalent to the Weisfeiler–Lehman test for distinguishing graph structures.
 - **CIN:** CIN (Bodnar et al., 2021) is a higher-order graph neural network inspired by the Weisfeiler–Lehman framework, which operates on cellular complexes to capture rich topological structures beyond pairwise node interactions.
 - **GMT:** GMT (Baek et al., 2021) is a graph neural network architecture that learns graph-level representations via hierarchical multiset pooling, enabling adaptive aggregation of node features and improving expressiveness for capturing complex graph structures.
- **Manifold-based Graph Geural Networks:** We compare DisRFM with four manifold-based general graph neural networks:
 - **dDGM:** dDGM (Borde et al., 2022) is a latent graph inference framework that models graph structure in continuous product manifolds, enabling the learning of expressive graph representations by jointly inferring latent relational structure and node embeddings.
 - **RieGrace:** RieGrace (Sun et al., 2023) is a self-supervised continual graph learning approach that adapts Riemannian representation spaces over time, enabling robust knowledge accumulation and transfer across evolving graph distributions.
 - **ProGDM:** ProGDM (Wang et al., 2024c) is a graph diffusion model that integrates mixed-curvature geometric spaces, enabling effective information propagation and representation learning across graphs with heterogeneous structural properties.
 - **D-GCN:** D-GCN (Sun et al., 2024) is a motif-aware Riemannian graph neural network that leverages generative–contrastive learning to capture higher-order structural patterns and geometric relationships in graph representations.
- **Graph Domain Adaptation method.** We compare DisRFM with seven graph domain adaptation methods:
 - **DEAL:** DEAL (Yin et al., 2022): addresses unsupervised domain adaptation for graph-level classification by learning domain-invariant graph representations through adversarial training, where a shared graph encoder is optimized to confuse a domain discriminator while preserving discriminative power on source labels.
 - **SGDA:** SGDA (Qiao et al., 2023) performs semi-supervised domain adaptation for graph transfer learning by jointly aligning feature representations and structural distributions across source and target domains, enabling effective knowledge transfer under limited target supervision.
 - **StruRW:** StruRW (Liu et al., 2023a) improves graph domain adaptation by re-weighting structural components to mitigate distributional shifts and enhance cross-domain representation alignment.
 - **A2GNN:** A2GNN (Liu et al., 2024a) rethinks information propagation for unsupervised graph domain adaptation by redesigning message-passing mechanisms to better align cross-domain graph representations.
 - **PA-BOTH:** PA-BOTH (Liu et al., 2024b) enhances graph domain adaptation through pairwise alignment of node representations and structural patterns across domains, effectively reducing distribution shifts and facilitating robust knowledge transfer between source and target graphs.

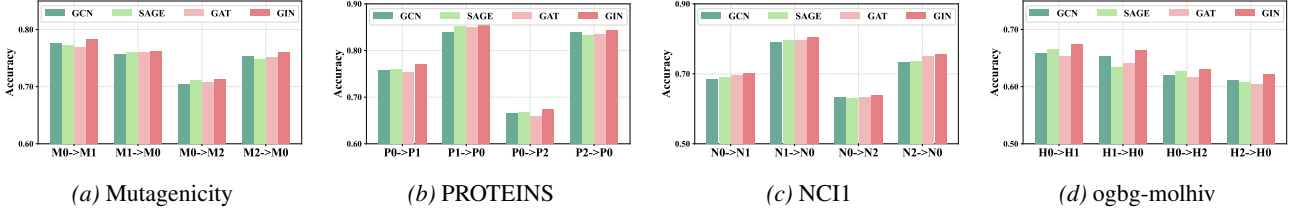
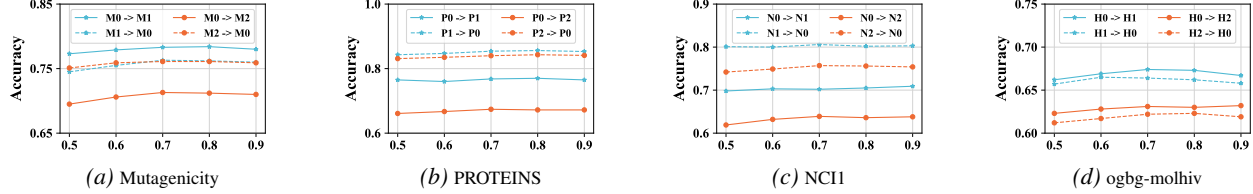


Figure 6. The performance with different GNN architectures on different datasets.


 Figure 7. Hyperparameter sensitivity analysis of confidence threshold ζ on the Mutagenicity, PROTEINS, NCI1 and ogbg-molhiv datasets.

- **GAA**: GAA (Fang et al., 2025) investigates attribute-driven graph domain adaptation by leveraging node attributes to guide representation alignment across domains, demonstrating that attribute information plays a critical role in mitigating domain shifts and improving transfer performance.
- **TDSS**: TDSS (Chen et al., 2025b) emphasizes graph smoothness as a key inductive bias for unsupervised graph domain adaptation, enforcing consistent representations among neighboring nodes to effectively reduce domain discrepancy and improve cross-domain generalization.
- **Manifold-based Domain Adaptation method.** We compare DisRFM with three manifold-based domain adaptation methods:
 - **GOTDA**: GOTDA (Long et al., 2022) formulates domain adaptation as an optimal transport problem on Grassmann manifolds, aligning subspace representations across domains to reduce distributional discrepancy and enable effective knowledge transfer.
 - **MASH**: MASH (Rustad et al., 2024) performs graph integration for diffusion-based manifold alignment by leveraging diffusion processes to align manifold structures across domains, facilitating coherent representation learning and cross-domain knowledge transfer.
 - **GeoAdapt**: GeoAdapt (Gharib et al., 2025) performs domain adaptation by aligning geometric moments via Siegel embeddings, enabling principled matching of higher-order distributional statistics across domains in a structured geometric space.

H.1. Implementation Details

We implement all baselines and conduct all experiments on NVIDIA A100 GPUs to ensure fair comparison. All methods are evaluated under identical hyperparameter settings as the proposed DisRFM, using the Adam optimizer with a learning rate of 1×10^{-4} , a weight decay of 1×10^{-12} , a hidden embedding dimension of 128, and three GNN layers. Following standard unsupervised domain adaptation protocols (Wu et al., 2020; Yin et al., 2022; Wang et al., 2025b), all baselines are trained on labeled source-domain data and evaluated on unlabeled target-domain data. We report classification accuracy on TUDataset benchmarks (e.g., PROTEINS, NCI1) and AUC scores on OGB datasets (e.g., ogbg-molhiv), with all results averaged over five independent runs.

I. Complexity Analysis

Here we analyze the computational complexity of the proposed DisRFM. The computational complexity primarily relies on the Riemannian graph convolution and manifold flow matching. For a given batch of graphs, $|\mathcal{E}|$ denotes the total number of edges. d is the embedding dimension. L denotes the layer number of the HGNN. $|\mathcal{V}|$ is the total number of nodes. B represents the batch size. The HGNN takes $\mathcal{O}(L \cdot (|\mathcal{E}| \cdot d + |\mathcal{V}| \cdot d^2))$ computational time, while the flow matching

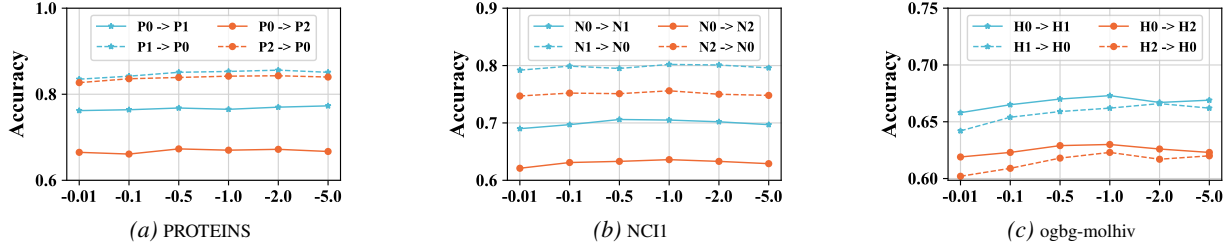


Figure 8. Hyperparameter sensitivity analysis of curve ratio c on the PROTEINS, NCI1 and ogbg-molhiv datasets.

and geometric constraints introduce an additional term of $\mathcal{O}(B^2 \cdot d)$ for coupling and alignment. As a result, the overall computational complexity of DisRFM is $\mathcal{O}(L \cdot (|\mathcal{E}| \cdot d + |\mathcal{V}| \cdot d^2) + B^2 \cdot d)$.

J. More experimental results

J.1. More performance comparison

In this section, we present additional experimental results comparing the proposed DisRFM with all baseline models across various datasets, as reported in Tables 8–15. We still can find that DisRFM consistently outperforms baselines on most cases, further demonstrating its effectiveness and robustness.

Additionally, we conduct experiments to evaluate the flexibility of the proposed DisRFM. Specifically, we replace the tangent space aggregation module of the HGCN (Liu et al., 2019) with different GNN backbones (i.e., GCN, SAGE and GAT), and present the results in Figure 6. The results show that GIN consistently outperforms other GNN architectures across most settings, indicating its stronger representational capacity. This observation further supports our choice of GIN as the default message passing mechanism to enhance the overall performance of DisRFM.

J.2. More Ablation study

To validate the effectiveness of the each component in DisRFM, we further conduct ablation studies on the PROTEINS, NCI1, and ogbg-molhiv datasets. Specifically, we evaluate five variants of DisRFM, including DisRFM w/o FM, DisRFM w/o RA, DisRFM w/o AA, and DisRFM w/o PE. The experimental results are reported in Tables 5, 6, and 7. From these results, we observe trends consistent with those summarized in Section 5.5.

J.3. More Sensitivity Analysis

In this section, we first investigate the sensitivity of the proposed DisRFM to the angular confidence threshold ζ on the Mutagenicity, PROTEINS, NCI1, and ogbg-molhiv datasets. The threshold ζ governs the reliability of target pseudo-labels by excluding ambiguous samples during angular alignment. Figure 7 reports the performance of DisRFM as ζ varies with the range of $\{0.5, 0.6, 0.7, 0.8, 0.9\}$. As shown in Figure 7, the performance consistently improves as ζ increases from 0.5 to 0.7, followed by a mild degradation at higher values. This behavior suggests that a low threshold allows noisy target samples to participate in angular alignment, leading to negative transfer, whereas an overly strict threshold excludes informative samples and weakens semantic guidance. Based on this trade-off, we set $\zeta = 0.7$ as the default value. We further analysis the sensitivity of DisRFM to the curvature parameter c on the PROTEINS, NCI1, and ogbg-molhiv datasets. The results, summarized in Figure 8, exhibit trends consistent with the analysis presented in Section 5.6.

Additionally, we provide sensitivity analyses of the proposed DisRFM with respect to balance coefficient (λ_1, λ_3) and (λ_2, λ_3) on the Mutagenicity dataset. The results are illustrated in Figures 9, from which we observe trends consistent with those discussed in Section 5.6.

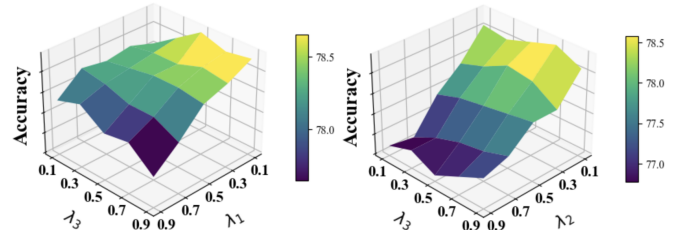


Figure 9. The model performance w.r.t. different combinations of λ_1 , λ_2 and λ_3 .

Riemannian Flow Matching for Disentangled Graph Domain Adaptation

Table 4. The results of ablation studies on the Mutagenicity dataset (source → target). **Bold** results indicate the best performance.

Methods	M0→M1	M1→M0	M0→M2	M2→M0	M0→M3	M3→M0	M1→M2	M2→M1	M1→M3	M3→M1	M2→M3	M3→M2
DisRFM w/o FM	76.2	73.6	69.6	74.0	65.3	66.2	77.2	81.1	66.3	69.3	71.2	73.6
DisRFM w/o RA	76.9	74.4	70.7	73.9	66.1	67.1	77.8	82.0	66.8	70.6	71.9	74.7
DisRFM w/o AA	76.4	74.0	70.2	73.5	65.7	66.0	77.0	81.3	65.9	69.5	71.3	73.8
DisRFM w/o PE	75.9	72.9	69.0	72.5	64.6	64.8	76.2	80.0	64.1	67.9	70.6	72.5
DisRFM	78.3	76.3	71.3	76.1	67.7	69.2	79.0	83.3	68.3	73.0	73.3	76.0

Table 5. The results of ablation studies on the PROTEINS dataset (source → target). **Bold** results indicate the best performance.

Methods	P0→P1	P1→P0	P0→P2	P2→P0	P0→P3	P3→P0	P1→P2	P2→P1	P1→P3	P3→P1	P2→P3	P3→P2
DisRFM w/o FM	74.6	82.6	64.9	81.7	72.0	80.9	65.3	72.3	72.7	71.9	72.9	59.9
DisRFM w/o RA	75.3	82.9	66.0	82.1	73.4	81.7	67.2	73.3	73.0	73.4	72.1	60.9
DisRFM w/o AA	75.1	83.0	65.7	81.5	72.9	81.5	66.1	72.7	71.6	72.7	73.0	60.3
DisRFM w/o PE	74.2	81.9	64.7	80.8	71.9	80.6	65.3	71.9	70.8	72.0	71.9	59.6
DisRFM	77.0	85.6	67.4	84.3	75.9	83.8	67.9	74.9	75.9	74.4	74.5	62.9

Table 6. The results of ablation studies on the NCI1 dataset (source → target). **Bold** results indicate the best performance.

Methods	N0→N1	N1→N0	N0→N2	N2→N0	N0→N3	N3→N0	N1→N2	N2→N1	N1→N3	N3→N1	N2→N3	N3→N2
DisRFM w/o FM	68.4	78.4	62.3	73.4	62.2	70.0	68.6	70.1	66.2	56.4	72.1	64.0
DisRFM w/o RA	68.9	78.2	62.6	72.9	63.2	71.3	69.2	70.7	66.4	57.2	72.6	64.5
DisRFM w/o AA	67.8	78.7	62.3	74.0	62.3	71.0	68.7	69.8	65.1	56.7	72.7	63.9
DisRFM w/o PE	67.0	77.6	62.0	71.7	62.0	70.2	67.9	69.3	64.0	56.4	71.9	63.2
DisRFM	70.2	80.6	63.9	75.7	64.6	72.6	70.7	71.9	68.0	58.2	74.4	65.6

Table 7. The results of ablation studies on the ogbg-molhiv dataset (source → target). **Bold** results indicate the best performance.

Methods	H0→H1	H1→H0	H0→H2	H2→H0	H0→H3	H3→H0	H1→H2	H2→H1	H1→H3	H3→H1	H2→H3	H3→H2
DisRFM w/o FM	65.1	64.7	60.8	60.0	64.3	58.3	67.2	66.1	70.8	65.9	74.8	68.2
DisRFM w/o RA	66.1	65.6	61.7	59.4	64.0	59.7	67.7	67.0	70.1	65.7	75.7	68.8
DisRFM w/o AA	64.9	64.3	59.8	58.8	63.8	58.0	66.5	66.3	69.9	64.6	74.3	67.5
DisRFM w/o PE	64.5	63.8	59.4	58.6	62.6	58.2	66.0	66.1	68.4	63.9	74.0	67.1
DisRFM	67.4	66.4	63.1	62.2	66.2	60.9	68.7	68.4	72.1	67.3	77.2	70.5

Table 8. The graph classification results (in %) on PROTEINS under node density domain shift (source→target). P0, P1, P2, and P3 denote the sub-datasets partitioned with node density. **Bold** results indicate the best performance.

Methods	P0→P1	P1→P0	P0→P2	P2→P0	P0→P3	P3→P0	P1→P2	P2→P1	P1→P3	P3→P1	P2→P3	P3→P2
WL subtree	69.1	59.7	61.2	75.9	41.6	83.5	61.5	72.7	24.7	72.7	63.1	62.9
GCN	73.7 ± 0.3	82.7 ± 0.4	57.6 ± 0.2	84.0 ± 1.3	24.4 ± 0.4	17.3 ± 0.2	57.6 ± 0.1	70.9 ± 0.7	24.4 ± 0.5	26.3 ± 0.1	37.5 ± 0.2	42.5 ± 0.8
GIN	71.8 ± 2.7	70.2 ± 4.7	58.5 ± 4.3	56.9 ± 4.9	74.2 ± 1.7	78.2 ± 3.3	63.3 ± 2.7	67.1 ± 3.8	35.9 ± 4.2	61.0 ± 2.4	71.9 ± 2.1	65.1 ± 1.0
GMT	73.7 ± 0.2	82.7 ± 0.1	57.6 ± 0.3	83.1 ± 0.5	75.6 ± 1.4	17.3 ± 0.6	57.6 ± 1.5	73.7 ± 0.6	75.6 ± 0.4	26.3 ± 1.2	75.6 ± 0.7	42.4 ± 0.5
CIN	74.1 ± 0.6	83.8 ± 1.0	60.1 ± 2.1	78.6 ± 3.1	75.6 ± 0.2	74.8 ± 3.7	63.9 ± 2.7	74.1 ± 0.6	57.0 ± 4.3	58.9 ± 3.3	75.6 ± 0.7	63.6 ± 1.0
PathNN	71.5 ± 1.6	67.1 ± 1.4	63.5 ± 1.1	54.2 ± 1.9	44.6 ± 1.3	45.6 ± 1.9	63.1 ± 2.3	63.5 ± 1.6	28.0 ± 2.2	49.1 ± 1.9	53.2 ± 2.6	58.9 ± 1.9
dDGM	72.5 ± 1.3	81.2 ± 1.5	64.6 ± 1.2	81.5 ± 1.4	59.8 ± 1.0	68.4 ± 1.5	66.2 ± 1.6	71.8 ± 0.8	50.8 ± 1.2	65.1 ± 1.8	67.5 ± 1.1	62.5 ± 1.5
RieGrace	75.0 ± 1.2	81.7 ± 1.1	67.6 ± 0.6	80.8 ± 0.8	61.6 ± 1.7	60.0 ± 1.2	65.9 ± 0.7	71.0 ± 1.3	59.8 ± 1.7	60.2 ± 1.3	65.7 ± 1.2	60.6 ± 1.5
ProGDM	74.4 ± 0.8	83.6 ± 0.7	66.8 ± 0.6	83.1 ± 0.9	52.6 ± 1.0	17.3 ± 1.0	63.7 ± 1.3	74.2 ± 1.2	33.0 ± 0.5	26.3 ± 1.0	65.9 ± 1.4	42.4 ± 1.0
D-GCN	73.7 ± 1.0	82.3 ± 1.2	57.6 ± 1.0	83.5 ± 1.3	42.4 ± 1.0	56.8 ± 1.3	58.7 ± 1.0	74.0 ± 1.1	48.2 ± 1.2	55.8 ± 2.1	42.2 ± 1.2	51.9 ± 1.8
DEAL	75.2 ± 1.2	78.8 ± 3.3	67.5 ± 2.1	74.5 ± 6.1	65.2 ± 2.2	76.2 ± 2.0	66.6 ± 0.9	73.7 ± 1.4	71.1 ± 1.8	69.9 ± 2.7	57.6 ± 1.5	65.7 ± 0.4
SGDA	64.2 ± 0.5	61.0 ± 0.7	66.9 ± 1.2	61.9 ± 0.9	65.4 ± 1.6	66.5 ± 1.0	64.6 ± 1.1	60.1 ± 0.5	66.3 ± 1.3	59.3 ± 0.8	66.0 ± 1.6	66.2 ± 1.3
StruRW	71.9 ± 2.3	82.6 ± 1.9	66.7 ± 1.8	74.5 ± 2.8	52.8 ± 1.9	57.3 ± 2.0	62.2 ± 2.4	63.3 ± 2.1	59.5 ± 1.6	56.3 ± 2.0	66.6 ± 2.3	52.4 ± 2.0
A2GNN	65.7 ± 0.6	65.9 ± 0.8	66.3 ± 0.9	65.6 ± 1.1	65.2 ± 1.4	65.6 ± 1.3	65.9 ± 1.7	65.8 ± 1.6	65.0 ± 1.5	66.1 ± 1.2	65.2 ± 1.9	65.9 ± 1.8
PA-BOTH	61.0 ± 0.8	61.2 ± 1.3	60.3 ± 0.6	66.7 ± 2.1	63.7 ± 1.5	61.9 ± 2.0	66.2 ± 1.4	69.9 ± 2.3	68.0 ± 0.7	69.4 ± 1.8	61.5 ± 0.4	67.6 ± 1.0
GAA	74.9 ± 1.3	83.5 ± 1.4	65.9 ± 1.3	82.3 ± 1.9	64.4 ± 1.7	55.2 ± 1.8	67.0 ± 1.7	74.3 ± 1.3	65.4 ± 1.9	58.7 ± 1.7	70.5 ± 2.1	57.5 ± 1.5
TDSS	73.9 ± 1.2	82.9 ± 1.3	57.8 ± 1.3	83.1 ± 1.2	60.4 ± 1.7	61.6 ± 2.0	58.1 ± 1.4	74.4 ± 1.5	62.7 ± 1.9	65.8 ± 1.0	58.2 ± 1.7	65.5 ± 1.0
GOTDA	74.5 ± 1.4	83.3 ± 1.3	64.5 ± 1.4	83.7 ± 0.7	52.3 ± 1.2	70.4 ± 0.7	65.0 ± 1.3	74.6 ± 1.5	38.6 ± 1.6	68.6 ± 1.0	64.3 ± 1.4	61.9 ± 1.3
MASH	74.7 ± 1.2	83.6 ± 1.3	62.6 ± 1.7	84.1 ± 0.8	47.1 ± 1.3	71.1 ± 0.9	60.9 ± 1.6	74.5 ± 1.2	49.3 ± 0.9	65.9 ± 1.3	64.7 ± 1.4	66.0 ± 2.0
GeoAdapt	74.1 ± 1.2	83.0 ± 1.4	66.4 ± 1.0	83.3 ± 1.2	68.5 ± 1.8	73.9 ± 2.2	65.9 ± 1.4	74.0 ± 1.4	67.8 ± 2.0	64.5 ± 1.9	68.7 ± 1.6	59.9 ± 2.3
DisRFM- \mathbb{E}^n	75.8 ± 0.7	83.3 ± 1.2	68.0 ± 1.1	83.2 ± 1.5	74.8 ± 2.0	82.1 ± 1.7	65.8 ± 0.5	73.9 ± 1.2	72.5 ± 1.4	72.0 ± 1.5	72.8 ± 1.9	62.2 ± 2.1
DisRFM- \mathbb{S}^n	76.1 ± 1.4	83.7 ± 1.5	68.3 ± 0.6	83.8 ± 1.6	75.6 ± 1.3	82.7 ± 1.8	67.0 ± 1.1	75.1 ± 0.6	74.1 ± 1.7	73.7 ± 1.4	73.3 ± 1.4	64.6 ± 1.1
DisRFM- \mathbb{H}^n	76.4 ± 1.7	84.1 ± 2.1	69.0 ± 1.4	84.3 ± 1.5	75.9 ± 1.1	83.9 ± 1.9	67.2 ± 1.8	75.5 ± 1.3	75.7 ± 2.0	74.4 ± 1.6	75.7 ± 1.7	66.1 ± 1.9

Table 9. The graph classification results (in %) on PROTEINS under edge density domain shift (source \rightarrow target). P0, P1, P2, and P3 denote the sub-datasets partitioned with edge density. **Bold** results indicate the best performance.

Methods	P0 \rightarrow P1	P1 \rightarrow P0	P0 \rightarrow P2	P2 \rightarrow P0	P0 \rightarrow P3	P3 \rightarrow P0	P1 \rightarrow P2	P2 \rightarrow P1	P1 \rightarrow P3	P3 \rightarrow P1	P2 \rightarrow P3	P3 \rightarrow P2
WL subtree	68.7	82.3	50.7	82.3	58.1	83.8	64.0	74.1	43.7	70.5	71.3	60.1
GCN	73.4 \pm 0.2	83.5 \pm 0.3	57.6 \pm 0.2	84.2 \pm 1.8	24.0 \pm 0.1	16.6 \pm 0.4	57.6 \pm 0.2	73.7 \pm 0.4	24.0 \pm 0.1	26.6 \pm 0.2	39.9 \pm 0.9	42.5 \pm 0.1
GIN	62.5 \pm 4.7	74.9 \pm 3.7	53.0 \pm 4.6	59.6 \pm 4.2	73.7 \pm 0.8	64.7 \pm 3.4	60.6 \pm 2.7	69.8 \pm 0.6	31.1 \pm 2.8	63.1 \pm 3.4	72.3 \pm 2.7	64.6 \pm 1.4
GMT	73.4 \pm 0.3	83.5 \pm 0.2	57.6 \pm 0.1	83.5 \pm 0.3	24.0 \pm 0.1	83.5 \pm 0.1	57.4 \pm 0.2	73.4 \pm 0.2	24.1 \pm 0.1	73.4 \pm 0.3	24.0 \pm 0.1	57.6 \pm 0.2
CIN	74.5 \pm 0.2	84.1 \pm 0.5	57.8 \pm 0.2	82.7 \pm 0.9	75.6 \pm 0.6	79.2 \pm 2.2	61.5 \pm 2.7	74.0 \pm 1.0	75.5 \pm 0.8	72.5 \pm 2.1	76.0 \pm 0.3	60.9 \pm 1.2
PathNN	72.7 \pm 1.3	80.8 \pm 1.6	63.5 \pm 2.5	68.1 \pm 1.1	43.2 \pm 1.6	25.3 \pm 1.5	60.2 \pm 1.7	66.0 \pm 1.3	33.1 \pm 2.9	38.5 \pm 1.1	49.8 \pm 1.4	54.3 \pm 1.1
dDGM	73.0 \pm 1.4	82.1 \pm 1.4	65.9 \pm 1.4	81.4 \pm 1.3	58.6 \pm 1.7	56.5 \pm 1.6	65.0 \pm 1.3	72.3 \pm 1.2	50.0 \pm 1.0	56.0 \pm 1.1	68.0 \pm 1.0	59.6 \pm 1.4
RieGrace	74.9 \pm 1.4	82.6 \pm 1.3	65.4 \pm 1.3	82.1 \pm 1.0	61.9 \pm 1.8	66.7 \pm 1.9	64.1 \pm 0.8	72.7 \pm 1.5	59.6 \pm 1.2	63.3 \pm 1.6	70.7 \pm 1.1	61.0 \pm 1.0
ProGDM	74.5 \pm 1.0	84.7 \pm 1.2	65.3 \pm 0.8	83.3 \pm 1.1	48.0 \pm 1.2	16.5 \pm 1.0	62.7 \pm 1.4	74.6 \pm 1.2	34.8 \pm 0.9	26.6 \pm 1.0	62.7 \pm 1.6	42.4 \pm 1.0
D-GCN	73.4 \pm 1.0	83.1 \pm 1.3	57.6 \pm 1.5	82.2 \pm 1.3	44.0 \pm 0.9	56.9 \pm 1.7	59.3 \pm 1.1	74.2 \pm 1.3	51.8 \pm 1.2	55.4 \pm 1.4	42.8 \pm 1.0	51.8 \pm 0.7
DEAL	74.1 \pm 0.3	78.8 \pm 2.3	65.1 \pm 1.8	79.1 \pm 3.4	63.7 \pm 2.7	67.3 \pm 5.3	69.0 \pm 0.9	74.2 \pm 1.6	60.8 \pm 2.4	70.6 \pm 2.8	71.3 \pm 5.7	65.9 \pm 0.9
SGDA	63.8 \pm 0.6	65.2 \pm 1.3	66.7 \pm 1.0	59.1 \pm 1.5	60.1 \pm 0.8	64.4 \pm 1.2	65.2 \pm 0.7	63.9 \pm 0.9	64.5 \pm 0.6	61.1 \pm 1.3	58.9 \pm 1.4	64.9 \pm 1.2
StruRW	72.6 \pm 2.2	84.5 \pm 1.7	66.2 \pm 2.2	72.5 \pm 2.4	48.9 \pm 2.0	56.5 \pm 2.3	63.1 \pm 1.8	64.4 \pm 2.4	55.8 \pm 2.0	56.6 \pm 2.4	67.0 \pm 2.6	42.4 \pm 2.0
A2GNN	65.4 \pm 1.3	66.3 \pm 1.1	65.2 \pm 1.4	66.3 \pm 1.2	65.4 \pm 0.7	65.9 \pm 0.9	66.9 \pm 1.3	65.4 \pm 1.2	65.6 \pm 0.9	65.5 \pm 1.2	66.1 \pm 2.0	66.0 \pm 1.8
PA-BOTH	63.1 \pm 0.7	67.2 \pm 1.1	64.3 \pm 0.5	72.1 \pm 1.8	66.3 \pm 0.7	64.1 \pm 1.2	69.7 \pm 2.1	67.5 \pm 1.4	61.2 \pm 1.4	67.7 \pm 2.3	61.2 \pm 1.6	65.5 \pm 0.6
GAA	75.4 \pm 1.3	82.8 \pm 1.4	66.9 \pm 1.8	83.5 \pm 1.5	64.2 \pm 1.9	56.0 \pm 2.2	67.5 \pm 1.0	74.5 \pm 1.3	60.1 \pm 1.6	60.3 \pm 1.5	72.4 \pm 1.5	58.1 \pm 1.4
TDSS	73.6 \pm 1.2	83.7 \pm 1.2	57.8 \pm 1.3	83.7 \pm 1.5	60.9 \pm 1.3	61.5 \pm 2.2	67.8 \pm 1.7	73.5 \pm 1.3	64.1 \pm 1.0	63.3 \pm 1.6	66.3 \pm 1.1	59.9 \pm 2.0
GOTDA	75.0 \pm 1.2	83.6 \pm 1.3	65.7 \pm 1.3	83.8 \pm 1.5	51.5 \pm 1.6	70.4 \pm 1.1	64.7 \pm 1.0	74.6 \pm 0.9	36.7 \pm 1.4	64.2 \pm 1.8	61.4 \pm 1.2	59.7 \pm 1.0
MASH	74.4 \pm 1.5	84.6 \pm 1.3	61.4 \pm 1.3	82.7 \pm 1.6	47.7 \pm 1.5	63.5 \pm 0.9	61.9 \pm 1.7	73.8 \pm 1.1	47.8 \pm 0.9	66.6 \pm 1.4	59.0 \pm 1.2	64.7 \pm 1.0
GeoAdapt	74.5 \pm 1.3	83.8 \pm 1.4	65.3 \pm 1.3	84.0 \pm 1.6	66.9 \pm 1.5	73.3 \pm 1.8	65.0 \pm 1.5	73.9 \pm 2.2	71.9 \pm 1.7	64.9 \pm 2.4	61.1 \pm 2.0	63.1 \pm 1.9
DisRFM- \mathbb{E}^n	76.0 \pm 0.7	82.9 \pm 1.3	66.7 \pm 0.3	82.0 \pm 1.3	71.1 \pm 1.6	81.2 \pm 1.8	67.0 \pm 1.0	73.2 \pm 0.8	72.9 \pm 1.5	71.1 \pm 2.1	71.6 \pm 1.1	61.7 \pm 1.7
DisRFM- \mathbb{S}^n	74.9 \pm 0.7	84.4 \pm 1.3	66.8 \pm 0.3	83.4 \pm 1.1	72.6 \pm 1.7	81.3 \pm 1.6	67.5 \pm 0.9	74.0 \pm 0.5	73.7 \pm 1.9	72.6 \pm 1.7	72.3 \pm 1.7	61.3 \pm 1.8
DisRFM- \mathbb{H}^n	77.0 \pm 1.3	85.6 \pm 1.5	67.4 \pm 1.4	84.3 \pm 2.1	75.9 \pm 2.0	83.8 \pm 1.7	67.9 \pm 1.6	74.9 \pm 1.3	75.9 \pm 1.5	74.4 \pm 1.9	74.5 \pm 1.4	62.9 \pm 1.7

Table 10. The classification results (in %) on the NCI1 dataset under node density domain shift (source \rightarrow target). N0, N1, N2, and N3 denote the sub-datasets partitioned with node density. **Bold** results indicate the best performance.

Methods	N0 \rightarrow N1	N1 \rightarrow N0	N0 \rightarrow N2	N2 \rightarrow N0	N0 \rightarrow N3	N3 \rightarrow N0	N1 \rightarrow N2	N2 \rightarrow N1	N1 \rightarrow N3	N3 \rightarrow N1	N2 \rightarrow N3	N3 \rightarrow N2
WL subtree	54.9	60.0	51.4	51.4	44.4	63.1	51.9	53.4	58.4	57.4	61.2	50.9
GCN	54.0 \pm 2.0	66.5 \pm 1.9	47.3 \pm 2.2	37.4 \pm 1.8	38.4 \pm 2.3	27.6 \pm 1.5	59.0 \pm 1.7	56.9 \pm 2.0	56.5 \pm 1.2	51.0 \pm 1.7	60.5 \pm 1.9	57.4 \pm 1.6
GIN	57.0 \pm 1.9	38.7 \pm 2.3	45.7 \pm 1.8	34.4 \pm 1.9	43.6 \pm 2.1	27.0 \pm 2.0	54.7 \pm 1.7	52.8 \pm 2.1	59.0 \pm 1.8	49.1 \pm 2.5	59.4 \pm 2.0	57.4 \pm 1.3
GMT	53.0 \pm 1.9	63.7 \pm 1.6	48.9 \pm 2.2	32.8 \pm 2.0	41.5 \pm 1.7	27.8 \pm 1.6	56.4 \pm 1.9	57.2 \pm 1.7	54.1 \pm 1.9	49.8 \pm 1.7	61.6 \pm 2.1	58.5 \pm 1.1
CIN	54.5 \pm 1.9	37.6 \pm 1.9	53.2 \pm 1.8	36.2 \pm 1.4	42.1 \pm 1.8	27.5 \pm 2.0	57.2 \pm 1.6	51.6 \pm 1.9	59.3 \pm 1.5	50.0 \pm 1.4	62.0 \pm 1.4	57.4 \pm 2.3
PathNN	56.8 \pm 2.5	62.8 \pm 2.1	52.7 \pm 2.2	64.5 \pm 1.2	50.6 \pm 1.8	37.4 \pm 2.1	59.2 \pm 1.4	58.6 \pm 1.5	60.2 \pm 1.8	53.1 \pm 2.1	60.9 \pm 1.2	57.6 \pm 1.5
dDGM	69.1 \pm 0.5	76.7 \pm 0.6	60.9 \pm 0.7	75.5 \pm 1.1	60.5 \pm 1.9	72.8 \pm 0.4	70.5 \pm 0.5	68.0 \pm 0.6	66.4 \pm 0.9	56.4 \pm 1.7	68.6 \pm 1.3	65.3 \pm 1.1
RieGrace	68.4 \pm 0.5	75.5 \pm 0.9	61.0 \pm 0.8	73.8 \pm 0.8	58.8 \pm 1.4	63.4 \pm 1.3	69.9 \pm 1.3	66.7 \pm 1.2	63.9 \pm 0.5	57.4 \pm 2.1	69.2 \pm 0.4	65.9 \pm 0.7
ProGDM	53.6 \pm 1.2	73.6 \pm 1.2	46.4 \pm 0.9	27.0 \pm 1.0	44.5 \pm 2.2	27.0 \pm 1.1	57.5 \pm 1.5	49.1 \pm 1.0	66.5 \pm 1.3	49.2 \pm 1.6	66.5 \pm 1.0	57.4 \pm 1.7
D-GCN	56.7 \pm 0.7	77.3 \pm 0.6	51.2 \pm 0.9	69.8 \pm 1.9	40.4 \pm 0.9	27.4 \pm 0.1	63.0 \pm 1.1	65.2 \pm 0.3	62.2 \pm 1.6	49.9 \pm 0.5	66.5 \pm 1.0	58.7 \pm 0.8
DEAL	70.6 \pm 0.6	77.4 \pm 0.8	62.9 \pm 1.2	74.5 \pm 0.5	62.6 \pm 4.4	70.3 \pm 1.6	69.4 \pm 0.6	70.0 \pm 0.7	66.3 \pm 0.6	62.4 \pm 1.4	74.0 \pm 0.6	66.6 \pm 1.0
SGDA	69.2 \pm 1.2	76.5 \pm 1.1	63.2 \pm 0.9	73.4 \pm 0.8	53.2 \pm 1.1	60.2 \pm 1.5	70.5 \pm 1.3	69.0 \pm 0.5	63.0 \pm 0.9	57.4 \pm 1.5	68.3 \pm 1.3	66.5 \pm 0.8
A2GNN	53.0 \pm 1.3	73.7 \pm 0.5	52.9 \pm 1.9	73.6 \pm 1.0	58.9 \pm 1.7	70.5 \pm 1.8	59.8 \pm 1.8	59.4 \pm 0.7	63.6 \pm 1.8	59.3 \pm 0.8	66.7 \pm 0.4	61.2 \pm 1.7
StruRW	67.3 \pm 0.7	77.0 \pm 2.0	62.1 \pm 1.0	73.9 \pm 0.6	53.6 \pm 2.5	62.6 \pm 1.7	69.7 \pm 0.5	68.3 \pm 0.3	62.7 \pm 2.1	62.1 \pm 2.0	68.3 \pm 1.2	67.1 \pm 0.5
PA-BOTH	51.2 \pm 0.5	75.4 \pm 1.0	42.8 \pm 0.1	64.2 \pm 1.9	35.8 \pm 1.1	55.3 \pm 2.1	61.6 \pm 2.1	53.4 \pm 1.7	64.4 \pm 1.0	50.9 \pm 1.1	66.7 \pm 0.4	57.5 \pm 0.2
GAA	70.6 \pm 0.9	78.8 \pm 0.6	63.7 \pm 0.5	74.5 \pm 0.9	62.9 \pm 0.7	72.7 \pm 0.7	70.6 \pm 0.3	69.0 \pm 0.8	66.7 \pm 0.8	62.0 \pm 1.8	69.4 \pm 1.1	66.9 \pm 0.5
TDSS	50.9 \pm 0.9	74.3 \pm 0.6	42.8 \pm 1.2	60.4 \pm 1.0	33.6 \pm 0.1	36.4 \pm 1.3	59.4 \pm 1.5	52.6 \pm 2.3	66.3 \pm 0.4	49.5 \pm 0.8	66.6 \pm 1.1	57.3 \pm 1.0
GOTDA	67.6 \pm 0.7	75.2 $\$										

Table 11. The classification results (in %) on the NCI1 dataset under edge density domain shift (source \rightarrow target). N0, N1, N2, and N3 denote the sub-datasets partitioned with edge density. **Bold** results indicate the best performance.

Methods	N0→N1	N1→N0	N0→N2	N2→N0	N0→N3	N3→N0	N1→N2	N2→N1	N1→N3	N3→N1	N2→N3	N3→N2
WL subtree	50.1	59.9	50.9	51.0	51.8	54.5	56.7	57.0	52.5	57.6	54.4	46.9
GCN	53.7 \pm 2.1	68.2 \pm 1.9	50.6 \pm 1.9	45.8 \pm 1.7	35.5 \pm 2.4	28.2 \pm 2.2	55.9 \pm 1.7	56.8 \pm 1.9	55.7 \pm 1.5	53.2 \pm 2.1	60.4 \pm 1.8	54.8 \pm 0.9
GIN	51.4 \pm 1.7	47.5 \pm 2.1	50.4 \pm 1.6	32.7 \pm 1.6	47.0 \pm 2.1	29.4 \pm 2.3	52.4 \pm 1.9	55.7 \pm 2.0	64.3 \pm 1.8	51.1 \pm 1.2	60.3 \pm 1.3	53.5 \pm 1.6
GMT	53.0 \pm 1.9	58.3 \pm 1.7	49.0 \pm 1.9	34.3 \pm 1.6	39.7 \pm 1.5	27.5 \pm 2.4	55.8 \pm 1.6	60.4 \pm 2.1	51.3 \pm 1.0	51.5 \pm 1.6	60.0 \pm 2.6	54.5 \pm 1.4
CIN	54.5 \pm 2.1	36.8 \pm 1.9	53.0 \pm 1.3	32.7 \pm 2.1	44.9 \pm 1.4	27.4 \pm 1.1	58.4 \pm 1.6	54.2 \pm 2.3	63.9 \pm 1.6	51.2 \pm 1.4	64.7 \pm 1.1	53.7 \pm 2.1
PathNN	56.4 \pm 1.4	65.5 \pm 1.4	54.6 \pm 1.5	60.9 \pm 1.8	46.7 \pm 2.1	35.5 \pm 1.9	57.6 \pm 1.8	60.6 \pm 1.2	61.9 \pm 1.8	53.9 \pm 2.0	65.1 \pm 1.8	52.5 \pm 1.5
dDGM	69.1 \pm 0.4	77.3 \pm 1.1	62.7 \pm 0.8	74.7 \pm 0.9	60.9 \pm 1.2	63.4 \pm 1.4	68.5 \pm 0.6	68.4 \pm 0.3	68.3 \pm 1.1	56.7 \pm 2.6	68.9 \pm 0.2	60.8 \pm 0.6
RieGrace	68.5 \pm 1.2	76.7 \pm 0.5	62.1 \pm 0.7	74.4 \pm 1.6	56.9 \pm 1.4	55.2 \pm 1.0	68.2 \pm 0.5	67.7 \pm 0.5	67.8 \pm 1.1	57.2 \pm 1.5	69.3 \pm 0.1	63.5 \pm 1.5
ProGDM	54.0 \pm 1.2	73.0 \pm 1.1	47.4 \pm 1.2	57.6 \pm 1.6	41.8 \pm 0.9	27.5 \pm 1.1	53.9 \pm 1.3	52.1 \pm 1.4	68.2 \pm 1.0	51.7 \pm 1.4	68.2 \pm 1.0	53.4 \pm 1.2
D-GCN	56.2 \pm 1.3	78.2 \pm 0.5	54.8 \pm 0.5	72.3 \pm 1.7	41.2 \pm 0.7	27.5 \pm 1.1	61.1 \pm 0.4	65.0 \pm 0.1	64.8 \pm 1.1	51.4 \pm 0.3	68.2 \pm 1.0	53.8 \pm 0.7
DEAL	70.3 \pm 0.4	80.2 \pm 0.6	62.9 \pm 1.7	74.7 \pm 3.9	61.9 \pm 2.6	70.7 \pm 3.7	67.5 \pm 0.7	69.7 \pm 1.0	67.6 \pm 0.4	63.4\pm1.3	73.2 \pm 0.3	64.2 \pm 0.9
SGDA	68.3 \pm 1.4	78.5 \pm 0.5	62.4 \pm 0.8	74.4 \pm 0.6	51.6 \pm 1.3	46.8 \pm 1.2	69.3 \pm 0.6	68.9 \pm 0.5	64.0 \pm 1.0	56.1 \pm 1.0	68.2 \pm 0.7	62.1 \pm 1.0
A2GNN	53.5 \pm 1.3	74.8 \pm 0.9	53.1 \pm 0.8	73.7 \pm 1.4	52.1 \pm 1.4	71.0 \pm 1.6	59.6 \pm 2.4	59.5 \pm 1.4	67.8 \pm 0.6	58.9 \pm 1.4	68.4 \pm 0.7	59.6 \pm 1.4
StruRW	66.4 \pm 1.0	76.7 \pm 1.9	63.2 \pm 0.5	75.2 \pm 1.2	53.1 \pm 1.3	53.5 \pm 1.4	68.5 \pm 0.7	67.9 \pm 1.3	65.5 \pm 2.1	59.7 \pm 1.6	66.7 \pm 0.9	62.6 \pm 1.4
PA-BOTH	49.4 \pm 0.8	75.1 \pm 1.5	48.1 \pm 2.5	65.5 \pm 1.6	40.3 \pm 2.0	55.4 \pm 1.2	60.1 \pm 1.1	55.8 \pm 2.1	68.2 \pm 2.0	51.5 \pm 0.5	68.4 \pm 0.3	54.0 \pm 1.4
GAA	70.0 \pm 1.1	80.4 \pm 1.0	63.5 \pm 0.6	75.4 \pm 1.3	63.8 \pm 0.6	71.4 \pm 0.5	69.7 \pm 0.4	68.3 \pm 0.5	69.6\pm0.3	61.4 \pm 1.2	69.6 \pm 0.7	63.2 \pm 0.5
TDSS	49.0 \pm 1.0	74.7 \pm 0.7	46.8 \pm 1.0	72.8 \pm 0.9	31.9 \pm 0.8	36.5 \pm 1.1	56.3 \pm 2.7	54.1 \pm 1.9	68.2 \pm 2.0	51.0 \pm 1.4	68.3 \pm 1.3	53.2 \pm 1.0
GOTDA	66.4 \pm 0.6	74.8 \pm 0.7	63.7 \pm 1.0	73.9 \pm 0.7	51.3 \pm 1.1	39.4 \pm 1.8	68.2 \pm 0.4	68.7 \pm 0.4	65.5 \pm 0.6	54.5 \pm 1.1	67.7 \pm 0.6	58.6 \pm 0.7
MASH	51.5 \pm 1.6	76.4 \pm 1.4	48.0 \pm 0.9	72.1 \pm 2.7	36.1 \pm 1.2	37.5 \pm 1.7	63.3 \pm 0.6	60.3 \pm 2.0	66.0 \pm 1.7	51.9 \pm 1.8	67.3 \pm 1.2	54.3 \pm 2.1
GeoAdapt	62.7 \pm 0.8	75.6 \pm 0.9	60.4 \pm 0.7	72.9 \pm 1.2	46.6 \pm 1.3	37.9 \pm 1.4	67.3 \pm 1.3	67.6 \pm 0.4	64.9 \pm 2.0	54.3 \pm 1.3	66.0 \pm 1.1	57.6 \pm 1.3
DisRFM- \mathbb{E}^n	69.5 \pm 0.6	80.3 \pm 0.6	63.2 \pm 1.2	73.4 \pm 1.5	63.2 \pm 1.5	70.6 \pm 1.2	69.7 \pm 0.6	70.5 \pm 0.4	64.9 \pm 1.6	57.3 \pm 0.5	73.4 \pm 0.4	64.4 \pm 0.4
DisRFM- \mathbb{S}^n	70.8\pm1.3	80.4 \pm 0.3	63.3 \pm 1.1	74.8 \pm 1.5	63.9 \pm 1.6	71.1 \pm 1.0	70.4 \pm 0.4	71.0 \pm 0.3	65.7 \pm 1.8	58.1 \pm 0.6	73.6 \pm 0.7	64.8 \pm 0.7
DisRFM- \mathbb{H}^n	70.2 \pm 1.3	80.6\pm1.5	63.9\pm1.0	75.7\pm1.1	64.6\pm1.2	72.6\pm1.7	70.7\pm1.4	71.9\pm0.7	68.0 \pm 0.4	58.2 \pm 0.7	74.4\pm0.4	65.6\pm1.2

Table 12. The classification results (in %) on the Mutagenicity dataset under node density domain shift (source \rightarrow target). M0, M1, M2, and M3 denote the sub-datasets partitioned with node density. **Bold** results indicate the best performance.

Methods	M0→M1	M1→M0	M0→M2	M2→M0	M0→M3	M3→M0	M1→M2	M2→M1	M1→M3	M3→M1	M2→M3	M3→M2
WL subtree	34.3	46.0	40.4	50.4	52.7	52.1	51.6	48.3	45.6	40.8	53.5	52.4
GCN	64.1 \pm 1.4	62.6 \pm 2.3	65.5 \pm 2.0	62.3 \pm 1.1	56.9 \pm 2.1	53.7 \pm 1.8	66.1 \pm 1.6	70.8 \pm 2.1	47.7 \pm 1.9	49.2 \pm 2.1	52.1 \pm 1.7	54.4 \pm 2.1
GIN	66.5 \pm 2.1	53.2 \pm 2.3	52.0 \pm 1.7	62.6 \pm 2.3	53.7 \pm 1.7	48.6 \pm 2.3	71.5 \pm 2.5	70.0 \pm 2.1	52.2 \pm 2.3	64.3 \pm 2.1	50.9 \pm 1.4	52.4 \pm 1.5
GMT	65.7 \pm 1.8	67.1 \pm 1.9	62.1 \pm 2.1	66.4 \pm 1.2	59.0 \pm 2.0	69.9 \pm 1.4	68.4 \pm 2.3	60.4 \pm 1.3	48.2 \pm 2.0	59.1 \pm 1.3	60.6 \pm 1.7	
CIN	65.1 \pm 1.7	52.9 \pm 2.3	66.0 \pm 1.7	69.8 \pm 2.0	55.2 \pm 1.5	55.1 \pm 1.3	66.0 \pm 1.6	69.9 \pm 2.1	54.9 \pm 1.8	57.8 \pm 1.5	46.7 \pm 2.0	51.8 \pm 1.1
PathNN	70.2 \pm 1.5	68.9 \pm 1.5	67.1 \pm 2.0	70.2 \pm 1.3	58.0 \pm 1.9	60.4 \pm 2.2	68.9 \pm 1.6	70.3 \pm 1.9	59.8 \pm 1.7	57.7 \pm 1.5	59.9 \pm 1.7	61.8 \pm 0.9
dDGM	79.1 \pm 0.4	71.1 \pm 1.2	70.3 \pm 0.5	73.3 \pm 0.3	63.9 \pm 0.3	67.1 \pm 1.3	78.3 \pm 1.2	82.7 \pm 1.2	66.2 \pm 0.4	72.8 \pm 1.0	72.1 \pm 1.0	76.8 \pm 1.3
RieGrace	78.5 \pm 1.3	70.1 \pm 1.2	70.6 \pm 1.4	72.4 \pm 0.6	62.8 \pm 1.3	68.3 \pm 1.5	77.2 \pm 1.3	82.0 \pm 0.3	65.0 \pm 1.2	73.3 \pm 1.9	71.1 \pm 0.4	76.2 \pm 0.6
ProGDM	75.2 \pm 1.2	71.5 \pm 1.6	69.0 \pm 1.1	70.3 \pm 1.1	55.7 \pm 1.4	68.6 \pm 1.7	70.4 \pm 1.1	76.0 \pm 1.0	56.6 \pm 1.3	48.9 \pm 2.1	57.8 \pm 1.1	59.9 \pm 1.3
D-GCN	75.2 \pm 0.5	69.2 \pm 1.3	67.9 \pm 0.4	69.6 \pm 1.1	56.3 \pm 1.1	58.4 \pm 1.6	70.6 \pm 0.3	76.8 \pm 0.5	56.1 \pm 1.2	55.1 \pm 1.1	58.1 \pm 0.5	62.5 \pm 1.4
DEAL	77.1 \pm 0.9	70.9 \pm 0.4	70.9 \pm 0.9	69.2 \pm 1.5	60.3 \pm 1.1	57.1 \pm 9.3	77.6 \pm 0.5	82.5 \pm 1.3	62.9 \pm 1.6	74.1 \pm 1.0	65.8 \pm 1.2	76.4 \pm 1.1
SGDA	77.5 \pm 0.6	71.4 \pm 0.6	69.7 \pm 0.5	72.2 \pm 1.4	65.5 \pm 0.8	60.0 \pm 0.7	78.8 \pm 1.4	82.8 \pm 1.3	67.2 \pm 0.6	65.8 \pm 1.6	70.9 \pm 1.4	73.2 \pm 0.9
A2GNN	73.5 \pm 1.9	70.4 \pm 1.0	66.1 \pm 1.5	69.8 \pm 0.9	60.4 \pm 1.1	66.4 \pm 1.8	69.0 \pm 0.7	72.3 \pm 1.5	56.3 \pm 1.6	71.1 \pm 2.2	57.9 \pm 1.4	66.0 \pm 1.7
StruRW	78.3 \pm 1.3	71.0 \pm 1.4	69.7 \pm 1.3	71.3 \pm 1.5	62.6 \pm 0.7	62.6 \pm 1.6	78.8 \pm 0.4	82.2 \pm 1.2	65.8 \pm 0.8	71.5 \pm 1.3	70.0 \pm 1.4	74.5 \pm 1.0
PA-BOTH	69.8 \pm 1.5	47.5 \pm 2.0	63.8 \pm 1.9	48.8 \pm 1.6	55.3 \pm 1.1	53.9 \pm 1.7	59.9 \pm 1.8	67.3 \pm 2.0	49.1 \pm 1.3	68.6 \pm 1.4	48.6 \pm 1.4	62.7 \pm 1.7
GAA	79.3 \pm 1.2	73.9 \pm 1.3	71.2 \pm 0.7	72.6 \pm 1.3	65.6 \pm 1.3	63.7 \pm 2.3	77.1 \pm 1.4	82.1 \pm 1.4	67.7 \pm 1.3	75.8 \pm 1.0	70.7 \pm 1.6	75.2 \pm 0.9
TDSS	63.6 \pm 1.3	50.3 \pm 1.1	56.7 \pm 1.6	51.1 \pm 1.4	54.7 \pm 1.0	58.5 \pm 1.7	60.1 \pm 1.3	70.1 \pm 2.3	48.6 \pm 1.5	68.5 \pm 1.6	49.5 \pm 1.3	59.3 \pm 2.0
GOTDA	77.3 \pm 1.3	71.7 \pm 1.5	69.9 \pm 1.7	71.3 \pm 1.7	65.3 \pm 1.2	67.0 \pm 2.3	77.8 \pm 1.3	81.6 \pm 1.2	65.7 \pm 1.6	64.7 \pm 1.4	71.0 \pm 1.1	71.1 \pm 1.6
MASH	76.1 \pm 1.3	67.0 \pm 1.6	66.9 \pm 1.3	69.9 \pm 1.8	54.3 \pm 1.2	55.1 \pm 2.6	75.1 \pm 1.6	80.0 \pm 1.5	55.1 \pm 1.7	63.7 \pm 1.5	58.4 \pm 1.2	64.9 \pm 1.6
GeoAdapt	76.9 \pm 1.5	71.4 \pm 1.2	68.7 \pm 1.4	71.4 \pm 1.5	60.1 \pm 1.3	65.0 \pm 2.4	77.2 \pm 1.3	81.1 \pm 1.5	63.4 \pm 1.4	64.2 \pm 2.1	69.3 \pm 1.3	70.6 \pm 1.6
DisRFM- \mathbb{E}^n	79.4 \pm 0.7	72.1 \pm 0.7	71.0 \pm 1.0	72.9 \pm								

Table 13. The classification results (in %) on the Mutagenicity dataset under edge density domain shift (source \rightarrow target). M0, M1, M2, and M3 denote the sub-datasets partitioned with edge density. **Bold** results indicate the best performance.

Methods	M0→M1	M1→M0	M0→M2	M2→M0	M0→M3	M3→M0	M1→M2	M2→M1	M1→M3	M3→M1	M2→M3	M3→M2
WL subtree	34.4	39.6	47.6	43.6	52.7	46.4	59.8	40.9	53.0	65.1	52.6	42.4
GCN	66.3 \pm 1.7	65.1 \pm 2.2	63.6 \pm 1.4	67.6 \pm 1.6	56.0 \pm 1.4	49.6 \pm 1.9	66.1 \pm 2.0	71.8 \pm 1.8	48.0 \pm 2.3	47.8 \pm 1.7	51.6 \pm 1.8	56.6 \pm 2.2
GIN	67.1 \pm 1.7	56.1 \pm 1.5	54.2 \pm 2.6	65.6 \pm 1.6	55.4 \pm 1.9	50.8 \pm 2.1	67.9 \pm 2.1	69.4 \pm 2.0	53.4 \pm 1.6	66.7 \pm 2.0	50.4 \pm 1.1	55.4 \pm 1.2
GMT	67.9 \pm 1.3	63.9 \pm 1.8	61.5 \pm 1.8	68.5 \pm 1.5	58.2 \pm 2.4	54.3 \pm 1.8	66.7 \pm 1.9	76.1 \pm 1.7	58.8 \pm 1.5	44.5 \pm 1.5	59.0 \pm 1.4	63.7 \pm 1.7
CIN	66.3 \pm 1.8	56.7 \pm 2.5	60.8 \pm 1.7	67.4 \pm 1.7	55.8 \pm 2.4	52.3 \pm 1.8	63.4 \pm 2.3	69.3 \pm 1.2	54.3 \pm 1.2	60.7 \pm 1.4	49.0 \pm 1.3	54.4 \pm 1.7
PathNN	68.9 \pm 1.9	65.9 \pm 1.8	62.9 \pm 1.7	69.2 \pm 1.8	58.1 \pm 1.6	59.9 \pm 1.4	67.7 \pm 1.6	70.0 \pm 2.1	56.3 \pm 1.8	62.8 \pm 1.9	59.2 \pm 1.6	63.7 \pm 1.2
dDGM	76.5 \pm 1.3	75.5 \pm 0.6	69.0 \pm 1.3	75.7 \pm 1.3	67.0 \pm 0.4	63.2 \pm 0.9	77.7 \pm 1.2	81.1 \pm 0.3	65.6 \pm 0.3	67.3 \pm 1.1	71.0 \pm 0.5	75.0 \pm 0.9
RieGrace	76.4 \pm 0.5	76.0 \pm 0.4	68.9 \pm 0.6	74.9 \pm 1.2	66.1 \pm 1.2	67.3 \pm 1.5	77.3 \pm 1.1	80.7 \pm 1.2	67.5 \pm 0.7	70.4 \pm 1.2	71.7 \pm 0.4	75.4 \pm 0.8
ProGDM	74.6 \pm 1.2	72.8 \pm 1.4	67.5 \pm 1.2	71.9 \pm 1.2	55.5 \pm 0.7	52.6 \pm 1.3	69.4 \pm 1.1	74.5 \pm 1.2	56.7 \pm 0.9	48.7 \pm 1.6	58.2 \pm 1.1	62.8 \pm 1.1
D-GCN	73.8 \pm 1.2	70.8 \pm 1.2	66.8 \pm 1.4	71.4 \pm 1.2	56.7 \pm 1.0	56.9 \pm 1.2	69.6 \pm 1.5	75.1 \pm 1.3	56.6 \pm 1.3	55.4 \pm 0.7	59.4 \pm 1.2	63.9 \pm 0.7
DEAL	76.6 \pm 1.6	72.7 \pm 0.6	70.6 \pm 1.2	70.9 \pm 0.9	60.2 \pm 2.1	55.6 \pm 1.5	77.8 \pm 1.0	80.7 \pm 0.5	63.4 \pm 0.9	67.6 \pm 1.1	66.3 \pm 0.7	74.8 \pm 1.1
SGDA	75.9 \pm 1.6	74.3 \pm 1.3	68.9 \pm 0.8	74.3 \pm 0.4	64.4 \pm 0.4	56.2 \pm 0.7	78.5 \pm 0.3	81.8 \pm 1.1	68.1 \pm 0.3	65.2 \pm 2.2	71.7 \pm 0.4	73.4 \pm 1.2
A2GNN	69.5 \pm 1.4	72.0 \pm 1.8	68.6 \pm 1.4	71.0 \pm 2.0	58.8 \pm 2.2	69.5 \pm 1.1	69.0 \pm 1.2	71.5 \pm 1.3	57.1 \pm 2.7	69.3 \pm 1.0	59.7 \pm 1.3	67.4 \pm 1.2
StruRW	76.1 \pm 1.5	74.1 \pm 1.6	69.0 \pm 1.3	73.9 \pm 1.5	62.1 \pm 1.0	58.9 \pm 2.0	78.0 \pm 1.3	80.8 \pm 1.2	66.4 \pm 0.7	67.8 \pm 0.8	71.9 \pm 0.3	74.9 \pm 1.0
PA-BOTH	74.7 \pm 1.1	51.4 \pm 1.0	65.3 \pm 1.3	51.4 \pm 1.0	52.2 \pm 1.5	56.8 \pm 1.1	57.1 \pm 1.1	66.7 \pm 1.0	48.9 \pm 2.4	66.9 \pm 1.3	48.1 \pm 2.5	60.7 \pm 1.7
GAA	77.5 \pm 1.2	75.7 \pm 1.2	70.0 \pm 1.2	74.5 \pm 0.7	66.5 \pm 1.3	66.7 \pm 1.1	76.7 \pm 1.3	80.9 \pm 0.7	67.9 \pm 1.4	72.7 \pm 0.8	71.7 \pm 1.0	75.2 \pm 1.4
TDSS	71.6 \pm 1.5	53.6 \pm 1.2	67.3 \pm 1.0	56.2 \pm 1.3	55.4 \pm 1.6	62.2 \pm 1.0	57.3 \pm 1.3	71.1 \pm 1.5	48.2 \pm 1.2	54.4 \pm 2.2	50.9 \pm 1.6	61.5 \pm 1.9
GOTDA	76.1 \pm 1.2	74.0 \pm 0.3	68.5 \pm 0.8	74.3 \pm 0.3	65.8 \pm 0.6	62.4 \pm 1.7	77.3 \pm 0.5	80.1 \pm 0.9	66.7 \pm 0.4	63.9 \pm 1.7	71.4 \pm 0.6	72.5 \pm 0.3
MASH	74.4 \pm 1.2	70.0 \pm 0.7	66.1 \pm 0.5	71.8 \pm 0.7	52.2 \pm 1.2	53.0 \pm 1.1	74.3 \pm 0.6	78.8 \pm 1.2	55.1 \pm 1.2	60.5 \pm 2.1	59.8 \pm 1.5	67.0 \pm 0.5
GeoAdapt	75.5 \pm 1.2	74.3 \pm 0.9	67.5 \pm 1.2	74.4 \pm 0.8	60.5 \pm 0.6	61.1 \pm 1.2	77.0 \pm 1.0	79.9 \pm 0.7	64.4 \pm 0.6	64.3 \pm 1.3	70.0 \pm 0.7	72.2 \pm 0.5
DisRFM- \mathbb{E}^n	77.6 \pm 0.4	75.5 \pm 0.5	70.2 \pm 1.2	75.5 \pm 1.0	66.1 \pm 0.3	66.8 \pm 4.7	77.9 \pm 0.4	82.3 \pm 0.1	67.0 \pm 0.8	69.9 \pm 3.2	71.8 \pm 0.2	74.4 \pm 0.4
DisRFM- \mathbb{S}^n	78.0 \pm 0.5	76.6\pm0.9	71.0 \pm 0.6	75.8 \pm 0.6	68.2\pm1.0	71.5\pm1.1	78.7 \pm 0.3	83.1 \pm 0.4	71.8\pm0.4	72.8 \pm 3.7	73.1 \pm 0.5	75.6 \pm 0.8
DisRFM- \mathbb{H}^n	78.3\pm0.7	76.3 \pm 1.4	71.3\pm0.4	76.1\pm1.3	67.7 \pm 0.9	69.2 \pm 1.5	79.0\pm1.4	83.3\pm1.5	68.3 \pm 1.9	73.0\pm1.3	73.3\pm1.4	76.0\pm1.6

Table 14. The classification results (in %) on the ogbg-molhiv dataset under node density domain shift (source \rightarrow target). H0, H1, H2, and H3 denote the sub-datasets partitioned with node density. **Bold** results indicate the best performance.

Methods	H0→H1	H1→H0	H0→H2	H2→H0	H0→H3	H3→H0	H1→H2	H2→H1	H1→H3	H3→H1	H2→H3	H3→H2
WL	49.6	51.8	54.0	54.7	48.2	48.9	50.6	51.9	38.1	51.0	51.8	50.7
GCN	57.8 \pm 1.9	57.4 \pm 2.1	56.5 \pm 1.3	54.2 \pm 1.2	54.5 \pm 1.7	51.9 \pm 1.7	61.8 \pm 2.0	55.2 \pm 1.3	49.8 \pm 1.4	56.6 \pm 1.3	61.5 \pm 1.1	56.8 \pm 1.7
GIN	59.1 \pm 1.6	53.3 \pm 1.6	50.0 \pm 1.7	54.8 \pm 1.8	56.8 \pm 1.6	50.7 \pm 1.4	55.2 \pm 1.3	58.7 \pm 1.4	57.0 \pm 1.8	49.6 \pm 1.7	53.1 \pm 1.3	55.3 \pm 1.6
GMT	51.1 \pm 1.6	57.2 \pm 1.7	50.6 \pm 1.2	55.9 \pm 1.9	58.4 \pm 1.4	53.4 \pm 1.7	56.1 \pm 1.6	57.6 \pm 1.3	60.9 \pm 1.7	54.5 \pm 2.0	55.4 \pm 1.6	51.2 \pm 1.8
CIN	52.3 \pm 1.6	53.4 \pm 1.5	54.0 \pm 1.9	57.5 \pm 1.8	56.5 \pm 1.4	51.1 \pm 1.9	55.8 \pm 1.4	63.6 \pm 1.8	48.7 \pm 1.6	56.8 \pm 1.6	49.3 \pm 1.2	52.8 \pm 1.3
PathNN	50.3 \pm 1.3	51.2 \pm 1.8	51.5 \pm 1.2	55.3 \pm 1.8	56.7 \pm 1.2	52.2 \pm 1.5	53.7 \pm 1.7	51.5 \pm 1.4	53.9 \pm 1.9	54.3 \pm 1.5	55.6 \pm 1.8	56.0 \pm 1.5
dDGM	65.9 \pm 0.4	66.5 \pm 0.6	62.4 \pm 0.6	62.3 \pm 0.4	62.3 \pm 1.8	59.4 \pm 1.3	69.3 \pm 0.5	68.5 \pm 1.0	71.9 \pm 0.7	64.7 \pm 0.6	76.3 \pm 0.4	67.4 \pm 0.4
RieGrace	66.1 \pm 0.6	65.6 \pm 0.4	62.9 \pm 1.0	61.1 \pm 1.2	62.2 \pm 1.4	58.5 \pm 1.0	69.3 \pm 1.3	69.4\pm1.4	71.8 \pm 0.8	66.7 \pm 0.9	71.9 \pm 0.9	67.7 \pm 0.5
ProGDM	59.4 \pm 1.2	62.0 \pm 1.2	59.7 \pm 1.2	62.1 \pm 0.8	58.4 \pm 0.9	59.6 \pm 0.9	61.1 \pm 1.3	61.8 \pm 1.2	60.1 \pm 1.2	60.1 \pm 1.1	60.1 \pm 0.8	59.1 \pm 0.9
D-GCN	60.4 \pm 1.6	59.6 \pm 1.7	60.0 \pm 0.8	57.5 \pm 1.1	60.6 \pm 1.9	56.0 \pm 1.2	60.1 \pm 0.9	61.0 \pm 0.9	65.0 \pm 1.0	58.6 \pm 1.6	65.2 \pm 2.0	62.1 \pm 0.9
DEAL	62.7 \pm 1.4	64.9 \pm 0.5	61.6 \pm 1.5	61.2 \pm 1.3	64.4 \pm 1.1	60.5 \pm 1.9	67.0 \pm 0.9	65.7 \pm 0.8	68.8 \pm 3.9	63.4 \pm 1.2	67.1 \pm 2.4	66.8 \pm 1.4
SGDA	67.2 \pm 1.5	67.9 \pm 1.3	62.4 \pm 1.5	61.7 \pm 1.4	59.4 \pm 1.9	57.7 \pm 0.8	69.5 \pm 1.3	67.9 \pm 0.7	71.0 \pm 0.9	64.8 \pm 0.8	75.1 \pm 1.4	67.6 \pm 0.5
A2GNN	61.9 \pm 0.9	61.0 \pm 0.7	62.7 \pm 1.3	60.1 \pm 0.7	63.5 \pm 1.9	61.1 \pm 0.8	64.3 \pm 1.1	61.8 \pm 0.8	63.4 \pm 1.5	61.0 \pm 0.9	63.8 \pm 1.8	66.5 \pm 1.3
StruRW	67.5 \pm 1.2	66.9 \pm 0.6	63.7 \pm 0.6	61.7 \pm 0.7	62.8 \pm 1.9	59.1 \pm 1.1	69.5 \pm 1.1	67.0 \pm 1.2	72.2 \pm 1.2	65.0 \pm 0.9	75.2 \pm 0.8	67.9 \pm 0.7
PA-BOTH	59.1 \pm 1.4	60.9 \pm 0.7	59.4 \pm 0.7	60.3 \pm 1.4	66.6 \pm 1.1	60.2 \pm 1.3	60.5 \pm 0.6	61.9 \pm 1.3	65.6 \pm 0.7	59.9 \pm 0.5	68.1 \pm 1.2	59.9 \pm 0.5
GAA	64.0 \pm 1.6	66.7 \pm 0.7	64.1 \pm 0.8	63.4 \pm 1.4	64.9 \pm 1.0	63.4 \pm 0.9	69.7 \pm 1.5	67.1 \pm 1.0	69.9 \pm 0.9	65.1 \pm 0.6	74.6 \pm 1.6	66.8 \pm 1.1
TDSS	61.4 \pm 0.6	60.4 \pm 1.2	60.9 \pm 0.5	60.5 \pm 1.3	62.3 \pm 0.6	60.3 \pm 0.5	61.1 \pm 0.4	62.1 \pm 1.3	61.6 \pm 0.8	62.2 \pm 0.6	61.4 \pm 0.9	61.4 \pm 0.4
GOTDA	65.5 \pm 1.5	66.4 \pm 0.5	62.4 \pm 1.4	61.3 \pm 0.8	61.1 \pm 0.9	58.7 \pm 1.3	68.1 \pm 1.4	67.4 \pm 0.5	69.0 \pm 1.2	64.6 \pm 0.8	74.8 \pm 0.6	67.4 \pm 0.6
MASH	62.2 \pm 1.0	61.2 \pm 1.0	62.2 \pm 0.9	60.7 \pm 0.6	63.1 \pm 0.5	60.6 \pm 1.1	66.2 \pm 0.8	64.2 \pm 1.0	67.9 \pm 1.2	63.2 \pm 1.7	71.4 \pm 0.5	63.8 \pm 0.8
GeoAdapt	65.8 \pm 0.6	65.5 \pm 0.6	62.3 \pm 0.7	59.8 \pm 0.6	62.3 \pm 1.0	57.6 \pm 0.7	68.3 \pm 0.5	66.8 \pm 0.4	68.5 \pm 0.4	63.8 \pm 0.7	74.0 \pm 0.6	67.0 \pm 0.4
DisRFM- \mathbb{E}^n	65.5 \pm 1.4	68.0 \pm 1.3	60.7<math									

Table 15. The classification results (in %) on the ogbg-molhiv dataset under edge density domain shift (source \rightarrow target). H0, H1, H2, and H3 denote the sub-datasets partitioned with edge density. **Bold** results indicate the best performance.

Methods	H0→H1	H1→H0	H0→H2	H2→H0	H0→H3	H3→H0	H1→H2	H2→H1	H1→H3	H3→H1	H2→H3	H3→H2
WL	45.4	54.9	44.9	46.7	54.4	52.2	53.7	46.0	56.1	45.3	51.1	50.8
GCN	57.5 \pm 1.8	58.0 \pm 1.5	56.1 \pm 2.1	54.3 \pm 1.2	54.1 \pm 1.4	50.9 \pm 1.4	61.2 \pm 1.6	54.8 \pm 1.9	54.9 \pm 2.1	56.6 \pm 1.4	65.4 \pm 2.0	58.1 \pm 1.6
GIN	58.1 \pm 1.1	55.3 \pm 1.2	49.7 \pm 1.5	55.2 \pm 2.2	55.5 \pm 1.9	50.5 \pm 2.0	55.1 \pm 1.3	58.8 \pm 1.2	56.6 \pm 1.6	50.0 \pm 1.1	56.8 \pm 1.8	56.2 \pm 1.6
GMT	50.7 \pm 1.0	57.5 \pm 1.7	51.1 \pm 2.1	58.8 \pm 1.5	59.8 \pm 1.4	52.0 \pm 1.4	57.0 \pm 1.8	55.4 \pm 1.0	54.0 \pm 1.7	54.9 \pm 1.0	58.1 \pm 1.3	52.0 \pm 1.3
CIN	51.8 \pm 1.4	54.1 \pm 1.7	53.6 \pm 1.4	57.3 \pm 1.6	56.9 \pm 1.7	53.9 \pm 1.3	54.5 \pm 1.7	63.6 \pm 2.1	54.2 \pm 1.2	56.9 \pm 1.8	57.6 \pm 1.3	58.7 \pm 1.2
PathNN	57.3 \pm 1.1	57.8 \pm 2.0	54.8 \pm 1.9	53.2 \pm 1.1	49.8 \pm 1.6	57.9 \pm 1.9	60.2 \pm 1.6	63.7 \pm 1.5	42.2 \pm 1.8	58.1 \pm 2.2	49.6 \pm 1.5	60.5 \pm 1.3
dDGM	66.3 \pm 0.5	65.9 \pm 1.4	61.6 \pm 0.7	60.9 \pm 1.3	59.9 \pm 0.5	59.3 \pm 0.7	67.9 \pm 1.3	68.1 \pm 1.2	70.5 \pm 1.4	66.4 \pm 0.6	74.3 \pm 1.3	66.7 \pm 0.7
RieGrace	66.8 \pm 1.4	64.5 \pm 0.6	62.2 \pm 0.8	60.3 \pm 1.3	63.7 \pm 1.5	59.4 \pm 1.0	67.4 \pm 1.4	67.2 \pm 0.6	70.8 \pm 0.6	67.6 \pm 1.3	73.1 \pm 1.3	68.6 \pm 0.6
ProGDM	58.5 \pm 1.3	61.5 \pm 1.2	59.0 \pm 1.2	60.7 \pm 1.1	58.2 \pm 1.1	58.4 \pm 1.4	61.6 \pm 1.2	62.8 \pm 1.2	60.7 \pm 1.1	60.4 \pm 1.2	62.3 \pm 1.2	61.2 \pm 0.5
D-GCN	61.9 \pm 0.9	59.3 \pm 1.5	59.6 \pm 1.6	57.8 \pm 1.9	60.6 \pm 2.9	56.8 \pm 1.9	59.5 \pm 1.7	61.0 \pm 0.8	65.1 \pm 1.0	59.8 \pm 2.3	64.5 \pm 1.3	61.4 \pm 1.4
DEAL	63.5 \pm 0.9	64.2 \pm 1.4	63.7\pm1.0	60.8 \pm 0.9	64.1 \pm 2.0	60.5 \pm 1.1	67.2 \pm 0.3	66.6 \pm 0.5	70.1 \pm 1.5	64.7 \pm 0.8	69.6 \pm 2.5	68.6 \pm 1.1
SGDA	66.7 \pm 1.4	66.0 \pm 0.6	63.4 \pm 1.4	61.4 \pm 1.3	60.6 \pm 1.9	59.8 \pm 0.8	67.3 \pm 1.3	67.8 \pm 1.5	71.0 \pm 0.6	67.1 \pm 1.3	76.1 \pm 1.4	69.5 \pm 1.4
A2GNN	62.6 \pm 1.4	61.1 \pm 0.8	63.2 \pm 1.5	61.0 \pm 1.1	65.1 \pm 1.4	60.1 \pm 1.3	64.1 \pm 1.6	61.7 \pm 1.0	64.7 \pm 1.0	61.6 \pm 0.7	65.5 \pm 1.8	63.7 \pm 1.8
StruRW	67.1 \pm 0.6	66.2 \pm 1.5	63.5 \pm 1.1	61.8 \pm 0.9	64.3 \pm 0.9	59.5 \pm 1.8	68.1 \pm 0.6	67.3 \pm 0.6	70.9 \pm 0.7	66.7 \pm 1.4	76.8 \pm 0.6	69.3 \pm 1.4
PA-BOTH	60.4 \pm 0.7	60.2 \pm 0.5	59.8 \pm 0.7	59.2 \pm 0.6	66.1 \pm 1.1	59.1 \pm 0.6	61.6 \pm 0.7	61.4 \pm 0.6	66.1 \pm 0.7	60.8 \pm 0.8	68.6 \pm 1.0	60.6 \pm 0.7
GAA	65.1 \pm 0.7	65.3 \pm 0.6	63.7 \pm 0.9	63.3 \pm 1.5	64.1 \pm 0.9	63.2 \pm 0.7	68.2 \pm 0.6	68.0 \pm 0.7	70.3 \pm 1.2	65.6 \pm 1.5	75.6 \pm 0.6	69.4 \pm 0.8
TDSS	62.2 \pm 1.5	59.5 \pm 0.5	61.5 \pm 0.6	59.5 \pm 0.5	62.7 \pm 0.8	59.5 \pm 1.3	61.7 \pm 1.3	62.8 \pm 1.4	62.0 \pm 1.0	63.0 \pm 0.4	62.0 \pm 1.0	61.7 \pm 1.3
GOTDA	65.8 \pm 0.7	65.9 \pm 0.5	61.6 \pm 0.6	60.8 \pm 0.3	61.4 \pm 1.1	59.1 \pm 1.1	67.0 \pm 0.5	67.5 \pm 0.5	69.8 \pm 1.1	65.8 \pm 0.5	75.7 \pm 0.4	69.2 \pm 0.4
MASH	64.8 \pm 0.9	59.0 \pm 1.4	62.2 \pm 1.6	58.4\pm1.7	64.3 \pm 0.6	60.1 \pm 1.1	65.0 \pm 0.5	63.9 \pm 0.6	68.5 \pm 0.8	64.4 \pm 0.7	72.8 \pm 0.9	65.0 \pm 1.1
GeoAdapt	67.0 \pm 0.8	64.5 \pm 0.7	61.4 \pm 0.6	59.4 \pm 1.4	62.9 \pm 2.0	57.9 \pm 1.1	66.9 \pm 0.6	67.2 \pm 1.3	70.8 \pm 0.7	65.6 \pm 0.8	74.9 \pm 1.3	68.3 \pm 0.4
DisRFM- \mathbb{E}^n	65.6 \pm 1.4	64.7 \pm 1.5	61.7 \pm 1.4	60.6 \pm 1.6	65.2 \pm 2.3	59.6 \pm 0.6	67.3 \pm 1.0	67.9 \pm 0.3	66.7 \pm 1.1	65.5 \pm 0.6	72.7 \pm 2.2	69.9 \pm 0.9
DisRFM- \mathbb{S}^n	66.5 \pm 0.9	66.0 \pm 1.0	62.3 \pm 1.4	60.8 \pm 1.6	64.6 \pm 2.7	61.0\pm1.1	69.1\pm1.2	70.6\pm1.7	71.3 \pm 3.2	66.8 \pm 1.8	74.4 \pm 2.6	69.6 \pm 0.7
DisRFM- \mathbb{H}^n	67.4\pm1.6	66.4\pm0.7	63.1 \pm 1.5	62.2\pm1.3	66.2\pm2.2	60.9 \pm 1.0	68.7 \pm 0.8	68.4 \pm 1.0	72.1\pm1.0	67.3\pm1.0	77.2\pm1.6	70.5\pm0.9